

OPTICAL SPECTROSCOPY AND VELOCITY DISPERSIONS OF GALAXY CLUSTERS FROM THE SPT-SZ SURVEY

J. RUEL¹, G. BAZIN^{2,3}, M. BAYLISS^{1,4}, M. BRODWIN⁵, R. J. FOLEY^{4,6,7}, B. STALDER⁴, K. A. AIRD⁸, R. ARMSTRONG⁹, M. L. N. ASHBY⁴, M. BAUTZ¹⁰, B. A. BENSON^{11,12}, L. E. BLEEM^{11,13,14}, S. BOCQUET^{2,3}, J. E. CARLSTROM^{11,12,13,14,15}, C. L. CHANG^{11,12,14}, S. C. CHAPMAN¹⁶, H. M. CHO¹⁷, A. CLOCCHIATTI¹⁸, T. M. CRAWFORD^{11,15}, A. T. CRITES^{11,15}, T. DE HAAN¹⁹, S. DESAI^{2,3}, M. A. DOBBS¹⁹, J. P. DUDLEY¹⁹, W. R. FORMAN⁴, E. M. GEORGE²⁰, M. D. GLADDERS^{11,15}, A. H. GONZALEZ²¹, N. W. HALVERSON²², N. L. HARRINGTON²⁰, F. W. HIGH^{11,15}, G. P. HOLDER¹⁹, W. L. HOLZAPFEL²⁰, J. D. HRUBES⁸, C. JONES⁴, M. JOY²³, R. KEISLER^{11,13}, L. KNOX²⁴, A. T. LEE^{20,25}, E. M. LEITCH^{11,15}, J. LIU^{2,3}, M. LUEKER^{20,26}, D. LUONG-VAN⁸, A. MANTZ¹¹, D. P. MARRONE²⁷, M. McDONALD¹⁰, J. J. McMAHON²⁸, J. MEHL^{11,15}, S. S. MEYER^{11,12,13,15}, L. MOCANU^{11,15}, J. J. MOHR^{2,3,29}, T. E. MONTROY³⁰, S. S. MURRAY⁴, T. NATOLI^{11,13}, D. NURGALIEV¹, S. PADIN^{11,15,26}, T. PLAGGE^{11,15}, C. PRYKE³¹, C. L. REICHARDT²⁰, A. REST³², J. E. RUHL³⁰, B. R. SALIWANCHIK³⁰, A. SARO², J. T. SAYRE³⁰, K. K. SCHAFFER^{11,12,33}, L. SHAW^{19,34}, E. SHIROKOFF^{20,26}, J. SONG²⁸, R. ŠUHADA², H. G. SPIELER²⁵, S. A. STANFORD^{24,35}, Z. STANISZEWSKI³⁰, A. A. STARSK⁴, K. STORY^{11,13}, C. W. STUBBS^{1,4}, A. VAN ENGELEN¹⁹, K. VANDERLINDE^{36,37}, J. D. VIEIRA^{6,26}, A. VIKHLININ⁴, R. WILLIAMSON^{11,15}, O. ZAHN^{20,38}, AND A. ZENTENO^{2,3}

¹ Department of Physics, Harvard University, 17 Oxford Street, Cambridge, MA 02138, USA; mbayliss@cfa.harvard.edu

² Department of Physics, Ludwig-Maximilians-Universität, Scheinerstr. 1, 81679 München, Germany

³ Excellence Cluster Universe, Boltzmannstr. 2, 85748 Garching, Germany

⁴ Harvard-Smithsonian Center for Astrophysics, 60 Garden Street, Cambridge, MA 02138, USA

⁵ Department of Physics and Astronomy, University of Missouri, 5110 Rockhill Road, Kansas City, MO 64110, USA

⁶ Astronomy Department, University of Illinois at Urbana-Champaign, 1002 W. Green Street, Urbana, IL 61801, USA

⁷ Department of Physics, University of Illinois Urbana-Champaign, 1110 W. Green Street, Urbana, IL 61801, USA

⁸ University of Chicago, 5640 South Ellis Avenue, Chicago, IL 60637, USA

⁹ Department of Physics and Astronomy, University of Pennsylvania, Philadelphia, PA 19104, USA

¹⁰ Kavli Institute for Astrophysics and Space Research, Massachusetts Institute of Technology, 77 Massachusetts Avenue, Cambridge, MA 02139, USA

¹¹ Kavli Institute for Cosmological Physics, University of Chicago, 5640 South Ellis Avenue, Chicago, IL 60637, USA

¹² Enrico Fermi Institute, University of Chicago, 5640 South Ellis Avenue, Chicago, IL 60637, USA

¹³ Department of Physics, University of Chicago, 5640 South Ellis Avenue, Chicago, IL 60637, USA

¹⁴ Argonne National Laboratory, 9700 S. Cass Avenue, Argonne, IL 60439, USA

¹⁵ Department of Astronomy and Astrophysics, University of Chicago, 5640 South Ellis Avenue, Chicago, IL 60637, USA

¹⁶ Institute of Astronomy, University of Cambridge, Madingley Road, Cambridge CB3 0HA, UK

¹⁷ NIST Quantum Devices Group, 325 Broadway Mailcode 817.03, Boulder, CO 80305, USA

¹⁸ Instituto de Astrofísica, Pontificia Universidad Católica, Chile

¹⁹ Department of Physics, McGill University, 3600 Rue University, Montreal, Quebec H3A 2T8, Canada

²⁰ Department of Physics, University of California, Berkeley, CA 94720, USA

²¹ Department of Astronomy, University of Florida, Gainesville, FL 32611, USA

²² Department of Astrophysical and Planetary Sciences and Department of Physics, University of Colorado, Boulder, CO 80309, USA

²³ Department of Space Science, VP62, NASA Marshall Space Flight Center, Huntsville, AL 35812, USA

²⁴ Department of Physics, University of California, One Shields Avenue, Davis, CA 95616, USA

²⁵ Physics Division, Lawrence Berkeley National Laboratory, Berkeley, CA 94720, USA

²⁶ California Institute of Technology, 1200 E. California Blvd., Pasadena, CA 91125, USA

²⁷ Steward Observatory, University of Arizona, 933 North Cherry Avenue, Tucson, AZ 85721, USA

²⁸ Department of Physics, University of Michigan, 450 Church Street, Ann Arbor, MI 48109, USA

²⁹ Max-Planck-Institut für extraterrestrische Physik, Giessenbachstr. 85748 Garching, Germany

³⁰ Physics Department, Center for Education and Research in Cosmology and Astrophysics, Case Western Reserve University, Cleveland, OH 44106, USA

³¹ Physics Department, University of Minnesota, 116 Church Street S.E., Minneapolis, MN 55455, USA

³² Space Telescope Science Institute, 3700 San Martin Drive, Baltimore, MD 21218, USA

³³ Liberal Arts Department, School of the Art Institute of Chicago, 112 S Michigan Avenue, Chicago, IL 60603, USA

³⁴ Department of Physics, Yale University, P.O. Box 208210, New Haven, CT 06520-8120, USA

³⁵ Institute of Geophysics and Planetary Physics, Lawrence Livermore National Laboratory, Livermore, CA 94551, USA

³⁶ Dunlap Institute for Astronomy & Astrophysics, University of Toronto, 50 St George Street, Toronto, ON, M5S 3H4, Canada

³⁷ Department of Astronomy & Astrophysics, University of Toronto, 50 St George Street, Toronto, ON, M5S 3H4, Canada

³⁸ Berkeley Center for Cosmological Physics, Department of Physics, University of California, and Lawrence Berkeley National Labs, Berkeley, CA 94720, USA

Received 2013 November 20; accepted 2014 July 10; published 2014 August 13

ABSTRACT

We present optical spectroscopy of galaxies in clusters detected through the Sunyaev–Zel’dovich (SZ) effect with the South Pole Telescope (SPT). We report our own measurements of 61 spectroscopic cluster redshifts, and 48 velocity dispersions each calculated with more than 15 member galaxies. This catalog also includes 19 dispersions of SPT-observed clusters previously reported in the literature. The majority of the clusters in this paper are SPT-discovered; of these, most have been previously reported in other SPT cluster catalogs, and five are reported here as SPT discoveries for the first time. By performing a resampling analysis of galaxy velocities, we find that unbiased velocity dispersions can be obtained from a relatively small number of member galaxies ($\lesssim 30$), but with increased systematic scatter. We use this analysis to determine statistical confidence intervals that include the effect of membership selection. We fit scaling relations between the observed cluster velocity dispersions and mass estimates from SZ and X-ray observables. In both cases, the results are consistent with the scaling relation between velocity dispersion and mass expected from dark-matter simulations. We measure a $\sim 30\%$ log-normal scatter in

dispersion at fixed mass, and a $\sim 10\%$ offset in the normalization of the dispersion–mass relation when compared to the expectation from simulations, which is within the expected level of systematic uncertainty.

Key words: catalogs – galaxies: clusters: general

Online-only material: color figures, machine-readable table

1. INTRODUCTION

Clusters of galaxies cause a distortion in the cosmic microwave background (CMB) from the inverse Compton scattering of the CMB photons with the hot intra-cluster gas, commonly called the Sunyaev–Zel’dovich (SZ) effect (Sunyaev & Zel’dovich 1972). SZ cluster surveys efficiently find massive, high-redshift clusters, primarily due to the redshift independence of the brightness of the SZ effect, with completed SZ surveys by the South Pole Telescope (SPT), Atacama Cosmology Telescope (ACT), and *Planck* having identified over 1000 clusters by their SZ distortion (see, e.g., Staniszewski et al. 2009; Vanderlinde et al. 2010; Williamson et al. 2011; Reichardt et al. 2013; Marriage et al. 2011; Hasselfield et al. 2013; Planck Collaboration et al. 2011, 2013). SZ-selected samples have provided a unique window into high-redshift cluster evolution (see, e.g., McDonald et al. 2012, 2013; Bayliss et al. 2013), and have also been used to constrain cosmological parameters (see, e.g., Benson et al. 2013; Reichardt et al. 2013).

In this paper, we report spectroscopic observations of galaxies associated with 61 galaxy clusters detected in the 2500 deg² SPT-SZ survey. This work is focused on measuring spectroscopic redshifts, which can inform cosmological studies in two ways. First, we present spectroscopically determined cosmological redshifts for most clusters. The measured spectroscopic redshifts are useful as a training set for photometric redshift measurements (High et al. 2010; Song et al. 2012).

Second, we present velocity dispersions, which are a potentially useful observable for measuring cluster mass (White et al. 2010; Saro et al. 2013). The cosmological constraints from the SPT-SZ cluster survey are currently limited by the uncertainty in the normalization of the SZ-mass relation (Benson et al. 2013; Reichardt et al. 2013). This motivates using multiple mass estimation methods, ideally in a joint likelihood analysis. Our group is pursuing X-ray observations (Andersson et al. 2011), weak lensing (High et al. 2012), and velocity dispersions to address the cluster mass calibration challenge. Currently, the relationship between the SZ observable and mass is primarily calibrated in a joint fit of SZ and X-ray data to a model that includes cosmological and scaling relation parameters (Benson et al. 2013). Like the SZ effect, X-ray emission is produced by the hot gas component of the cluster, so velocity dispersions and weak lensing are important for assessing any systematic biases from gas-based proxies. Velocity dispersions also have the advantage of being obtainable from ground-based telescopes up to high redshift.

The velocities of SPT cluster galaxies presented here are primarily derived from our spectroscopic measurements of 61 massive galaxy clusters. These data are used to produce 48 velocity dispersions for clusters with more than 15 member galaxies, several of which we have already presented elsewhere (Brodwin et al. 2010; Foley et al. 2011; Williamson et al. 2011; McDonald et al. 2012; Stalder et al. 2013; Reichardt et al. 2013; Bayliss et al. 2013). These are, for the most part, the data obtained through 2011 in our ongoing spectroscopy program. We also list dispersions collected from the literature, including observations of 14 clusters that were also detected by ACT and

targeted for spectroscopic followup by the ACT collaboration (Sifón et al. 2013).

This paper is organized as follows. We describe the observations and observing strategy in Section 2. In Section 3, we present our results, including the individual galaxy velocities and cluster velocity dispersions, and we investigate the phase-space galaxy selection using a stacking analysis. In Section 4, we use a resampling analysis to calculate cluster redshift and dispersion uncertainties that take the effect of the membership selection into account. We explore the properties of our sample of velocity dispersions by comparing them with SZ-based SPT masses, X-ray temperatures, and X-ray-derived masses in Section 5. The evaluation of our observing strategy and outstanding questions are summarized in the conclusion, Section 6.

Throughout this paper, we define M_{500c} (M_{200c}) as the mass contained within R_{500c} (R_{200c}), the radius from the cluster center within which the average density is 500 (200) times the critical density at the cluster redshift. Conversion between M_{500c} and M_{200c} is made assuming an NFW density profile and the Duffy et al. (2008) mass–concentration relation. We report uncertainties at the 68% confidence level, and we adopt a WMAP7 + BAO + H_0 flat Λ CDM cosmology with $\Omega_M = 0.272$, $\Omega_\Lambda = 0.728$, and $H_0 = 70.2 \text{ km s}^{-1} \text{ Mpc}^{-1}$ (Komatsu et al. 2011).

2. OBSERVATIONS

2.1. South Pole Telescope

Most of the galaxy clusters for which we report spectroscopic observations were published as SPT cluster detections (and new discoveries) in Vanderlinde et al. (2010), Williamson et al. (2011), and Reichardt et al. (2013); we refer the reader to those publications for details of the SPT observations. In Table 1, we give the SPT identification (ID) of the clusters and their essential SZ properties. This includes the right ascension and declination of the SZ center, the cluster redshift, and the SPT detection significance ξ . We also report the SPT cluster mass estimate, $M_{500c, \text{SPT}}$, as reported in Reichardt et al. (2013), for those clusters at redshift $z \geq 0.3$, the redshift threshold used in the SPT cosmological analysis. As described in Reichardt et al. (2013), the SPT mass estimate is measured from the SPT SZ significance and X-ray measurements, where available, while accounting for the SPT selection, and marginalizing over all uncertainties in cosmology and the cluster observable scaling relations. The last columns indicate the source of the spectroscopy, our own measurements for 61 clusters, and a literature reference for 19 of them. Five clusters have data from both sources.

There are 11 clusters that do not appear in prior SPT publications, and are presented here as SPT detections for the first time. Five of them are new discoveries (identified with * in Table 1), and the other six were previously published as ACT detections (Marriage et al. 2011, identified with ** in Table 1). These SPT detections will be reported in an upcoming cluster catalog from the full 2500 deg² SPT-SZ survey.

One cluster, SPT-CL J0245-5302, is detected by SPT at high significance; however, because of its proximity to a bright point

Table 1
SPT Properties and Source of Spectroscopic Data

SPT ID	ID and Coordinates			ξ	$M_{500c, \text{SPT}}$ ($10^{14} h_{70}^{-1} M_{\odot}$)	Source of Spectroscopy	
	R.A. (J2000 deg)	Decl. (J2000 deg)	z			This Work	Literature
SPT-CL J0000-5748	0.2496	-57.8066	0.702	5.48	4.29 ± 0.71	✓	
SPT-CL J0014-4952*	3.6969	-49.8772	0.752	8.87	5.14 ± 0.86	✓	
SPT-CL J0037-5047*	9.4441	-50.7971	1.026	6.93	3.64 ± 0.79	✓	
SPT-CL J0040-4407	10.2048	-44.1329	0.350	19.34	10.18 ± 1.32	✓	
SPT-CL J0102-4915	15.7294	-49.2611	0.870	39.91	15.69 ± 1.89		1
SPT-CL J0118-5156*	19.5990	-51.9434	0.705	5.97	3.39 ± 0.82	✓	
SPT-CL J0205-5829	31.4437	-58.4856	1.322	10.54	4.79 ± 1.00	✓	
SPT-CL J0205-6432	31.2786	-64.5461	0.744	6.02	3.29 ± 0.79	✓	
SPT-CL J0232-5257**	38.1876	-52.9578	0.556	8.65	5.04 ± 0.89		1
SPT-CL J0233-5819	38.2561	-58.3269	0.663	6.64	3.71 ± 0.86	✓	
SPT-CL J0234-5831	38.6790	-58.5217	0.415	14.65	7.64 ± 1.50	✓	
SPT-CL J0235-5121**	38.9468	-51.3516	0.278	9.78	...		1
SPT-CL J0236-4938**	39.2477	-49.6356	0.334	5.80	3.39 ± 0.89		1
SPT-CL J0240-5946	40.1620	-59.7703	0.400	9.04	5.29 ± 1.07	✓	
SPT-CL J0245-5302	41.3780	-53.0360	0.300	✓	
SPT-CL J0254-5857	43.5729	-58.9526	0.437	14.42	7.46 ± 1.46	✓	
SPT-CL J0257-5732	44.3516	-57.5423	0.434	5.40	3.14 ± 0.86	✓	
SPT-CL J0304-4921**	46.0619	-49.3612	0.392	12.75	7.32 ± 1.04		1
SPT-CL J0317-5935	49.3208	-59.5856	0.469	5.91	3.46 ± 0.89	✓	
SPT-CL J0328-5541	52.1663	-55.6975	0.084	7.08	...		3
SPT-CL J0330-5228**	52.7287	-52.4698	0.442	11.57	6.36 ± 1.00		1
SPT-CL J0346-5439**	56.7247	-54.6505	0.530	9.25	5.07 ± 0.93		1
SPT-CL J0431-6126	67.8393	-61.4438	0.059	6.40	...		2
SPT-CL J0433-5630	68.2522	-56.5038	0.692	5.35	2.89 ± 0.82	✓	
SPT-CL J0438-5419	69.5749	-54.3212	0.422	22.88	10.82 ± 1.39	✓	1
SPT-CL J0449-4901*	72.2742	-49.0246	0.790	8.91	4.57 ± 0.86	✓	
SPT-CL J0509-5342	77.3360	-53.7045	0.462	6.61	5.36 ± 0.71	✓	1
SPT-CL J0511-5154	77.9202	-51.9044	0.645	5.63	3.61 ± 0.96	✓	
SPT-CL J0516-5430	79.1480	-54.5062	0.294	9.42	...	✓	
SPT-CL J0521-5104	80.2983	-51.0812	0.675	5.45	3.46 ± 0.96		1
SPT-CL J0528-5300	82.0173	-53.0001	0.769	5.45	3.18 ± 0.61	✓	1
SPT-CL J0533-5005	83.3984	-50.0918	0.881	5.59	2.68 ± 0.61	✓	
SPT-CL J0534-5937	83.6018	-59.6289	0.576	4.57	2.71 ± 1.00	✓	
SPT-CL J0546-5345	86.6541	-53.7615	1.066	7.69	5.25 ± 0.75	✓	1
SPT-CL J0551-5709	87.9016	-57.1565	0.424	6.13	3.75 ± 0.54	✓	
SPT-CL J0559-5249	89.9245	-52.8265	0.609	9.28	6.79 ± 0.86	✓	1
SPT-CL J0658-5556	104.6317	-55.9465	0.296	39.05	...		4
SPT-CL J2012-5649	303.1132	-56.8308	0.055	5.99	...		2
SPT-CL J2022-6323	305.5235	-63.3973	0.383	6.58	3.82 ± 0.89	✓	
SPT-CL J2032-5627	308.0800	-56.4557	0.284	8.14	...	✓	
SPT-CL J2040-4451	310.2468	-44.8599	1.478	6.28	3.21 ± 0.79	✓	
SPT-CL J2040-5725	310.0631	-57.4287	0.930	6.38	3.25 ± 0.75	✓	
SPT-CL J2043-5035	310.8285	-50.5929	0.723	7.81	4.71 ± 1.00	✓	
SPT-CL J2056-5459	314.2199	-54.9892	0.718	6.05	3.68 ± 0.89	✓	
SPT-CL J2058-5608	314.5893	-56.1454	0.606	5.02	2.64 ± 0.79	✓	
SPT-CL J2100-4548	315.0936	-45.8057	0.712	4.84	2.71 ± 0.93	✓	
SPT-CL J2104-5224	316.2283	-52.4044	0.799	5.32	3.04 ± 0.89	✓	
SPT-CL J2106-5844	316.5210	-58.7448	1.131	22.08	8.36 ± 1.71	✓	
SPT-CL J2118-5055	319.7291	-50.9329	0.625	5.62	3.43 ± 0.93	✓	
SPT-CL J2124-6124	321.1488	-61.4141	0.435	8.21	4.68 ± 0.96	✓	
SPT-CL J2130-6458	322.7285	-64.9764	0.316	7.57	4.46 ± 0.96	✓	
SPT-CL J2135-5726	323.9158	-57.4415	0.427	10.43	5.68 ± 1.11	✓	
SPT-CL J2136-4704	324.1175	-47.0803	0.425	6.17	4.04 ± 0.96	✓	
SPT-CL J2136-6307	324.2334	-63.1233	0.926	6.25	3.18 ± 0.75	✓	
SPT-CL J2138-6007	324.5060	-60.1324	0.319	12.64	6.75 ± 1.32	✓	
SPT-CL J2145-5644	326.4694	-56.7477	0.480	12.30	6.39 ± 1.25	✓	
SPT-CL J2146-4633	326.6473	-46.5505	0.932	9.59	5.36 ± 1.07	✓	
SPT-CL J2146-4846	326.5346	-48.7774	0.623	5.88	3.64 ± 0.93	✓	
SPT-CL J2148-6116	327.1798	-61.2791	0.571	7.27	4.04 ± 0.89	✓	
SPT-CL J2155-6048	328.9851	-60.8072	0.539	5.24	2.82 ± 0.82	✓	
SPT-CL J2201-5956	330.4727	-59.9473	0.098	13.99	...		5
SPT-CL J2248-4431	342.1907	-44.5269	0.351	42.36	17.97 ± 2.18	✓	
SPT-CL J2300-5331	345.1765	-53.5170	0.262	5.29	...	✓	
SPT-CL J2301-5546	345.4688	-55.7758	0.748	5.19	3.11 ± 0.96	✓	

Table 1
(Continued)

ID and Coordinates						Source of Spectroscopy	
SPT ID	R.A. (J2000 deg)	Decl. (J2000 deg)	z	ξ	$M_{500c, \text{SPT}}$ ($10^{14} h_{70}^{-1} M_{\odot}$)	This Work	Literature
SPT-CL J2325-4111	351.3043	-41.1959	0.358	12.50	7.29 ± 1.07	✓	
SPT-CL J2331-5051	352.9584	-50.8641	0.575	8.04	5.14 ± 0.71	✓	
SPT-CL J2332-5358	353.1040	-53.9733	0.402	7.30	6.50 ± 0.79	✓	
SPT-CL J2337-5942	354.3544	-59.7052	0.776	14.94	8.14 ± 1.14	✓	
SPT-CL J2341-5119	355.2994	-51.3328	1.002	9.65	5.61 ± 0.82	✓	
SPT-CL J2342-5411	355.6903	-54.1887	1.075	6.18	3.00 ± 0.50	✓	
SPT-CL J2344-4243	356.1847	-42.7209	0.595	27.44	12.50 ± 1.57	✓	
SPT-CL J2347-5158*	356.9423	-51.9766	0.869	✓	
SPT-CL J2351-5452	357.8877	-54.8753	0.384	4.89	3.18 ± 1.04		6
SPT-CL J2355-5056	358.9551	-50.9367	0.320	5.89	4.07 ± 0.57	✓	
SPT-CL J2359-5009	359.9208	-50.1600	0.775	6.35	3.54 ± 0.54	✓	

Notes. SPT ID of each cluster, right ascension and declination of its SZ center, and redshift z (from Tables 4 and 5, for reference). Also given are the SPT significance ξ and the SZ-based SPT mass, marginalized over cosmological parameters as in Reichardt et al. (2013), for those clusters at $z \geq 0.3$, except for two, as described in Section 2.1. Clusters marked with ** are reported here as SPT detections for the first time, and those with * are new discoveries.

References. (1) Sifón et al. 2013; (2) Girardi et al. 1996; (3) Struble & Rood (1999); (4) Barrena et al. 2002; (5) Katgert et al. 1998; (6) Buckley-Geer et al. 2011.

source (<8 arcmin away), it is not included in the official catalog. SPT-CL J2347-5158 had a higher SPT significance in early maps of the survey, but has $\xi < 4.0$ in the 2500 deg² survey. The SPT significance and mass are not given for these two clusters.

2.2. Optical Spectroscopy

The spectroscopic observations presented in this work are the first of our ongoing follow-up program. The data were taken from 2008 to 2012 using the Gemini Multi Object Spectrograph (GMOS; Hook et al. 2004) on Gemini South, the Focal Reducer and low dispersion Spectrograph (FORS2; Appenzeller et al. 1998) on VLT Antu, the Inamori Magellan Areal Camera and Spectrograph (IMACS; Dressler et al. 2006) on Magellan Baade, and the Low Dispersion Survey Spectrograph (LDSS3³⁹; Allington-Smith et al. 1994) on Magellan Clay.

In order to place a large number of slitlets in the central region of the cluster, most of the IMACS observations were conducted with the Gladders Image-Slicing Multi-slit Option (GISMO⁴⁰). GISMO optically remaps the central region of the IMACS field of view (roughly 3.5×3.2) to sixteen evenly spaced regions of the focal plane, allowing for a large density of slitlets in the cluster core while minimizing slit collisions on the CCD.

Details about the observations pertaining to each cluster, including the instrument, optical configuration, number of masks, total exposure time, and measured spectral resolution, are listed in Table 2.

Optical and infrared follow-up imaging observations of SPT clusters are presented alongside our group's photometric redshift methodology in High et al. (2010), Song et al. (2012) and Desai et al. (2012). Those photometric redshifts (and in a few cases, spectroscopic redshifts from the literature) were used to guide the design of the spectroscopic observations. Multislit masks were designed using the best imaging available to us, usually a combination of ground-based *griz* (on Blanco/MOSAIC II, Magellan/IMACS, Magellan/LDSS3, or

BVRI on Swope) and *Spitzer*/IRAC $3.6 \mu\text{m}$. In addition, spectroscopic observations at Gemini and VLT were preceded by at least one-band (*r* or *i*) pre-imaging for relative astrometry, and two-band (*r* and *i*) pre-imaging for red-sequence target selection in the cases where the existing imaging was not deep enough. The exposure times for this pre-imaging were chosen to reach a magnitude depth for galaxy photometry of $m^* + 1$ at 10σ at the cluster redshift.

In designing the multislit masks, top priority for slit placement was given to bright red-sequence galaxies (the red sequence of SPT clusters is discussed in the context of photometric redshifts in High et al. 2010; Song et al. 2012), as defined by their distance to either a theoretical or an empirically fit red-sequence model. The details varied depending on the quality of the available imaging, the program, and the prioritization weighting scheme of the instrument's mask-making software. In many of the GISMO observations, blue galaxies were given higher priority than faint red galaxies because, especially at high redshift, they were expected to be more likely to yield a redshift. The results from the different red-sequence weighting schemes are very similar, and few emission lines are found, even at $z \gtrsim 1$ (Brodwin et al. 2010; Foley et al. 2011; Stalder et al. 2013, these articles also provide more details about the red-sequence nature of spectroscopic members). The case of SPT-CL J2040-4451 at $z = 1.478$ is different and redshifts were only obtained for emission-line galaxies (Bayliss et al. 2013). In all cases, non-red-sequence objects were used to fill out any remaining space in the mask.

The dispersers and filters, listed in Table 2, were chosen (within the uncertainty on the photo- z) to obtain low- to medium-resolution spectra covering at least the wavelengths of the main spectral features that we use to identify the galaxy redshifts: [O II] emission, and the Ca II H&K absorption lines and break.

The spectroscopic exposure times (also in Table 2) for GMOS and FORS2 observations were chosen to reach $S/N = 5$ ($S/N = 3$) per spectral element just below the 4000 Å break for a red galaxy of magnitude $m^* + 1$ ($m^* + 0.5$) at $z < 1$ ($z > 1$). Under the conditions prevailing at the telescope during classical observing, the exposure times for the Magellan observations

³⁹ <http://www.lco.cl/telescopes-information/magellan/instruments/ldss-3>

⁴⁰ <http://www.lco.cl/telescopes-information/magellan/instruments/imacs/gismo/gismoquickmanual.pdf>

Table 2
Observations

SPT ID	z	UT Date	Instrument	Disperser/Filter	Masks	N	t_{exp} (h)	Res. (Å)
SPT-CL J0000-5748	0.702	2010 Sep 7	GMOS-S	R150_G5326	2	26	1.33	23.7
SPT-CL J0014-4952	0.752	2011 Aug 21	FORS2	GRIS_300I/OG590	2	29	2.83	13.5
SPT-CL J0037-5047	1.026	2011 Aug 22	FORS2	GRIS_300I/OG590	2	18	5.00	13.5
SPT-CL J0040-4407	0.350	2011 Sep 29	GMOS-S	B600_G5323	2	36	1.17	5.7
SPT-CL J0118-5156	0.705	2011 Sep 28	GMOS-S	R400_G5325, N&S	2	14	2.53	9.0
SPT-CL J0205-5829	1.322	2011 Sep 25	IMACS	Gri-300-26.7/WB6300-950, f/2	1	9	11.00	5.2
SPT-CL J0205-6432	0.744	2011 Sep 30	GMOS-S	R400_G5325, N&S	2	15	2.67	9.0
SPT-CL J0233-5819	0.664	2011 Sep 29	GMOS-S	R400_G5325, N&S	1	10	1.33	9.0
SPT-CL J0234-5831	0.415	2010 Oct 8	IMACS/GISMO	Gra-300-4.3/Z1-430-675, f/4	1	22	1.50	6.5
SPT-CL J0240-5946	0.400	2010 Oct 9	IMACS/GISMO	Gra-300-4.3/Z1-430-675, f/4	1	25	1.00	6.4
SPT-CL J0245-5302	0.300	2011 Sep 29	GMOS-S	B600_G5323	2	29	0.83	7.0
SPT-CL J0254-5857	0.437	2010 Oct 8	IMACS/GISMO	Gra-300-4.3/Z1-430-675, f/4	1	35	1.50	6.9
SPT-CL J0257-5732	0.434	2010 Oct 9	IMACS/GISMO	Gra-300-4.3/Z1-430-675, f/4	1	22	1.50	6.6
SPT-CL J0317-5935	0.469	2010 Oct 9	IMACS/GISMO	Gra-300-4.3/Z1-430-675, f/4	1	17	1.63	6.6
SPT-CL J0433-5630	0.692	2011 Jan 28	IMACS/GISMO	Gri-300-17.5/Z2-520-775, f/2	1	22	1.00	5.7
SPT-CL J0438-5419	0.422	2011 Sep 28	GMOS-S	R400_G5325	1	18	0.75	9.0
SPT-CL J0449-4901	0.790	2011 Jan 28	IMACS/GISMO	Gri-300-26.7/WB6300-950, f/2	1	20	1.63	5.6
SPT-CL J0509-5342	0.462	2009 Dec 12	GMOS-S	R150_G5326	2	18	1.00	23.7
		2012 Mar 23	FORS2	GRIS_300V/GG435	1	4	2.37	13.7
SPT-CL J0511-5154	0.645	2011 Sep 30	GMOS-S	R400_G5325, N&S	2	15	2.67	9.0
SPT-CL J0516-5430	0.294	2010 Sep 17	IMACS/GISMO	Gra-300-4.3/Z1-430-675, f/4	2	48	1.67	6.7
SPT-CL J0528-5300	0.769	2010 Jan 13	GMOS-S	R150_G5326	2	20	3.00	23.7
SPT-CL J0533-5005	0.881	2008 Dec 5	LDSS3	VPH-Red	1	4	0.63	5.4
SPT-CL J0534-5937	0.576	2008 Dec 5	LDSS3	VPH-Red	1	3	0.45	5.5
SPT-CL J0546-5345	1.066	2010 Feb 11	IMACS/GISMO	Gri-300-26.7/WB6300-950, f/2	1	21	3.00	5.7
SPT-CL J0551-5709	0.424	2010 Sep 17	IMACS/GISMO	Gra-300-4.3/Z1-430-675, f/4	2	34	1.42	6.8
SPT-CL J0559-5249	0.609	2009 Dec 7	GMOS-S	R150_G5326	2	37	1.33	23.7
SPT-CL J2022-6323	0.383	2010 Oct 9	IMACS/GISMO	Gra-300-4.3/Z1-430-675, f/4	1	37	1.17	6.7
SPT-CL J2032-5627	0.284	2010 Oct 8	IMACS/GISMO	Gra-300-4.3/Z1-430-675, f/4	1	31	1.17	6.8
SPT-CL J2040-4451	1.478	2012 Sep 15	IMACS	Gri-300-26.7, f/2	2	14	11.30	9.3
SPT-CL J2040-5725	0.930	2010 Aug 13	IMACS/GISMO	Gri-300-26.7/WB6300-950, f/2	1	5	3.00	5.0
SPT-CL J2043-5035	0.723	2011 Aug 27	FORS2	GRIS_300I/OG590	2	21	4.00	13.5
SPT-CL J2056-5459	0.719	2010 Aug 14	IMACS/GISMO	Gri-300-26.7/WB6300-950, f/2	1	12	2.00	5.3
SPT-CL J2058-5608	0.607	2011 Oct 1	GMOS-S	R400_G5325	2	9	1.67	9.0
SPT-CL J2100-4548	0.712	2011 Jul 23	FORS2	GRIS_300I/OG590	2	19	1.50	13.5
SPT-CL J2104-5224	0.799	2011 Jul 21	FORS2	GRIS_300I/OG590	2	23	2.83	13.5
SPT-CL J2106-5844	1.131	2010 Dec 8	FORS2	GRIS_300I/OG590	1	15	3.00	13.5
		2010 Jun 7	IMACS/GISMO	Gri-300-26.7/WB6300-950, f/2	1	4	8.00	4.5
SPT-CL J2118-5055	0.625	2011 May 26	FORS2	GRIS_300I/OG590	2	22	1.33	13.5
		2011 Sep 27	GMOS-S	R400_G5325, N&S	1	3	1.20	9.0
SPT-CL J2124-6124	0.435	2009 Sep 25	IMACS/GISMO	Gra-300-4.3/Z1-430-675, f/4	1	24	1.50	7.0
SPT-CL J2130-6458	0.316	2010 Sep 17	IMACS/GISMO	Gra-300-4.3/Z1-430-675, f/4	2	47	2.00	7.1
SPT-CL J2135-5726	0.427	2010 Sep 16	IMACS/GISMO	Gra-300-4.3/Z1-430-675, f/4	1	33	1.00	6.8
SPT-CL J2136-4704	0.425	2011 Sep 29	GMOS-S	R400_G5325	2	24	1.67	9.0
SPT-CL J2136-6307	0.926	2010 Aug 14	IMACS/GISMO	Gri-300-26.7/WB6300-950, f/2	1	10	2.00	5.0
SPT-CL J2138-6007	0.319	2010 Sep 17	IMACS/GISMO	Gra-300-4.3/Z1-430-675, f/4	1	34	1.50	6.8
SPT-CL J2145-5644	0.480	2010 Sep 16	IMACS/GISMO	Gra-300-4.3/Z1-430-675, f/4	2	37	2.92	7.4
SPT-CL J2146-4633	0.931	2011 Sep 25	IMACS	Gri-300-26.7/WB6300-950, f/2	1	17	3.00	4.7
SPT-CL J2146-4846	0.623	2011 Oct 1	GMOS-S	R400_G5325	2	26	2.33	9.0
SPT-CL J2148-6116	0.571	2009 Sep 25	IMACS/GISMO	Gra-300-4.3/Z1-430-675, f/4	1	30	1.50	7.1
SPT-CL J2155-6048	0.539	2011 Oct 1	GMOS-S	R400_G5325	2	25	1.50	9.0
SPT-CL J2248-4431	0.351	2009 Jul 12	IMACS/GISMO	Gra-300-4.3/Z1-430-675, f/4	1	15	1.33	10.9
SPT-CL J2300-5331	0.262	2010 Oct 8	IMACS/GISMO	Gra-300-4.3/Z1-430-675, f/4	1	24	1.00	6.8
SPT-CL J2301-5546	0.748	2010 Aug 14	IMACS/GISMO	Gri-300-26.7/WB6300-950, f/2	1	11	2.00	5.4
SPT-CL J2325-4111	0.358	2011 Sep 28	GMOS-S	B600_G5323	2	33	1.00	5.7
SPT-CL J2331-5051	0.575	2008 Dec 5	LDSS3	VPH-Red	2	6	1.00	5.5
		2010 Sep 9	GMOS-S	R150_G5326	2	28	1.00	23.7
		2010 Oct 9	IMACS/GISMO	Gra-300-4.3/Z2-520-775, f/4	2	62	3.50	6.7
SPT-CL J2332-5358	0.403	2009 Jul 12	IMACS/GISMO	Gri-200-15.0/WB5694-9819, f/2	1	24	1.50	18.1
		2010 Sep 5	FORS2	GRIS_300V	2	29	4.38	13.7
SPT-CL J2337-5942	0.776	2010 Aug 14	GMOS-S	R150_G5326	2	19	3.00	23.7
SPT-CL J2341-5119	1.003	2010 Aug 14	GMOS-S	R150_G5326	2	15	6.00	23.7
SPT-CL J2342-5411	1.075	2010 Sep 9	GMOS-S	R150_G5326	1	11	3.00	23.7
SPT-CL J2344-4243	0.595	2011 Sep 30	GMOS-S	R400_G5325	2	32	2.33	9.0
SPT-CL J2347-5158	0.869	2010 Aug 13	IMACS/GISMO	Gri-300-26.7/WB6300-950, f/2	1	12	2.50	5.0
SPT-CL J2355-5056	0.320	2010 Sep 17	IMACS/GISMO	Gra-300-4.3/Z1-430-675, f/4	1	37	1.50	7.0
SPT-CL J2359-5009	0.775	2009 Nov 22	GMOS-S	R150_G5326	2	7	1.33	23.7
		2010 Aug 14	IMACS/GISMO	Gri-300-26.7/WB6300-950, f/2	1	22	2.00	5.4

Notes. The instruments used for our observations are IMACS on Magellan Baade, LDSS3 on Magellan Clay, GMOS-S on Gemini South, and FORS2 on VLT Antu. The UT date of observation, details of the configuration, and the number of observed multislit masks are given, as well as the number of member redshifts retrieved from the observation ($N \equiv N_{\text{members}}$), and the total spectroscopic exposure time for all masks, t_{exp} , in hours. The spectral resolution is the FWHM of sky lines in Angstroms, measured in the science exposures.

were determined by a combination of experience, real-time quick-look reductions, and airmass limitations.

2.2.1. Data Processing

We used the COSMOS reduction package⁴¹ (Kelson 2003) for CCD reductions of IMACS and LDSS3 data, and standard IRAF routines and XIDL⁴² routines for GMOS and FORS2. Flux calibration and telluric line removal were performed using the well-exposed continua of spectrophotometric standard stars (Wade & Horne 1988; Foley et al. 2003). Wavelength calibration is based on arc lamp exposures, obtained at night in between science exposures in the case of IMACS and LDSS3, and during daytime in the same configuration as for science exposures for GMOS and FORS2. In the case of daytime arc frames, the wavelength calibration was refined using sky lines in the science exposures.

The redshift determination was performed using cross-correlation with the *fabtemp97* template in the RVSAO package for IRAF (Kurtz & Mink 1998) or a proprietary template fitting method using the SDSS DR2 templates, and validated by agreement with visually identified absorption or emission features. A single method was used for each cluster depending on the reduction workflow, and both perform similarly. Comparison between the redshifts obtained from the continuum and emission-line redshifts, when both are available from the same spectrum, shows that the uncertainties on individual redshifts (twice the RVSAO uncertainty, see e.g., Quintana et al. 2000) correctly represent the statistical uncertainty of the fit.

2.3. A Few- N_{members} Spectroscopic Strategy

Modern multi-object spectrographs use slit masks, so that the investment in telescope time is quantized by how many masks are allocated to each cluster. The optimization problem is, therefore, to allocate the observation of m masks across n clusters so as to minimize the uncertainty on the ensemble cluster mass normalization.

We pursue a strategy for spectroscopic observations informed by the expectation (from N -body simulations; see, e.g., Kasun & Evrard 2005; White et al. 2010; Saro et al. 2013) that line-of-sight projection effects induce an unavoidable intrinsic scatter of 12% in log dispersion ($\ln \sigma$) at fixed mass, implying a 35% scatter in dynamical mass (Saro et al. 2013, see Equation (15) of the present paper). As this 35% intrinsic scatter needs to be added to the dynamical mass uncertainty of any one cluster, for the purpose of mass calibration, obtaining coarser dispersions on more clusters is more informative than measuring higher-precision velocity dispersions on a few clusters. Considering the results of those simulations and the experience encapsulated in the velocity dispersion literature (e.g., Girardi et al. 1993), we have adopted a target of $N_{\text{members}} \sim 20\text{--}30$, where N_{members} is the number of spectroscopic member galaxies in a cluster. This target range of N_{members} can be obtained by observing two masks per cluster on the spectrographs available to us.⁴³ The use

of a red-sequence selection to target likely cluster members is a necessary feature of this strategy, as a small number of multislit masks only allows us to target a small fraction of the galaxies in the region of the sky around the SZ center.

In discussions throughout this paper, we often use a $N_{\text{members}} \geq 15$ cut. We note that this number is chosen somewhat arbitrarily for the conservative exclusion of systems with very few members. As we will see in the resampling analysis of Section 4, no special statistical transition happens at $N_{\text{members}} = 15$, and dispersions with fewer members could potentially be used for reliable mass estimates.

Recent simulations and our data suggest that this choice of few-member strategy may increase the scatter due to systematics in the measured dispersions. This is discussed in Section 4.1.

3. RESULTS

3.1. Individual Galaxy Redshifts

The full sample of redshifts for both member and non-member galaxies is available in electronic format. In Table 3, we present a subset composed of central galaxies, for the 50 clusters where we have the central galaxy redshift. We have visually selected the central galaxy for each cluster to be a large, bright, typically cD-type galaxy that is close to the SZ center and that appears to be central to the distribution of galaxies. For each galaxy, the table lists the SPT ID of the associated cluster, a galaxy ID, right ascension and declination, the redshift and redshift-measurement method, and notable spectral features.

3.2. Cluster Redshifts and Velocity Dispersions

Table 4 lists the cluster redshifts and velocity dispersions measured from the galaxy redshifts.

The cluster redshift z is the biweight average (Beers et al. 1990) of member galaxy redshifts (see below) with an uncertainty given by the standard error, as explained in Section 4.2. Once the cluster redshift is computed, the galaxy proper velocities v_i are obtained from their redshifts z_i by $v_i = c(z_i - z)/(1 + z)$ (Danese et al. 1980). The velocity dispersion σ_{BI} is the square root of the biweight sample variance of proper velocities, the uncertainty of which we found to be well described by $0.92\sigma_{\text{BI}}/\sqrt{N_{\text{members}} - 1}$ when including the effect of membership selection (Section 4.2; see Section 4.1 for the formula of the biweight sample variance). We also report the dispersion σ_G determined from the gapper estimator, which is a preferred measurement, according to Beers et al. (1990), for those clusters with fewer than 15 member redshifts.

The cluster redshifts and velocity dispersions are calculated using only galaxies identified as members, where membership is established using iterative 3σ clipping on the velocities (Yahil & Vidal 1977; Mamon et al. 2010; Saro et al. 2013). The center at each iteration of 3σ clipping is the biweight average, and σ is calculated from the biweight variance, or the gapper estimator in the case where there are fewer than 15 members. We do not make a hard velocity cut; the initial estimate of σ used in the iterative clipping is determined from the galaxies located within 4000 km s^{-1} of the center, in the rest frame.

Figure 1 shows the velocity histogram for each cluster with 15 members or more, as well as an indication of emission-line objects and our determination of member and non-member galaxies.

Some entries in Table 4 have a star-shaped flag \star in the SPT ID column, which highlights possibly less reliable dispersion

⁴¹ <http://code.obs.carnegiescience.edu/cosmos>

⁴² <http://www.ucolick.org/~xavier/IDL/>

⁴³ Some of the observations presented here depart from this model and have only one slitmask with correspondingly fewer members. In some cases the second mask has yet to be observed, while in others observations were undertaken with different objectives (e.g., the identification and characterization of high-redshift clusters, the follow-up of bright sub-millimeter galaxies, and long slit observations from the early days of our follow-up program). Finally, some clusters of special interest were targeted with more than two masks.

Table 3
Galaxy Redshifts

Associated SPT ID	Galaxy ID	Galaxy R.A. (J2000 deg)	Galaxy Decl. (J2000 deg)	z	z Method	Spectral Features
SPT-CL J0000-5748	J000059.99-574832.7	0.2500	-57.8091	0.7007 ± 0.0002	template	[O II], Ca II H&K
SPT-CL J0037-5047	J003747.30-504718.9	9.4471	-50.7886	1.0302 ± 0.0002	template	Ca II H&K
SPT-CL J0118-5156	J011824.76-515628.6	19.6032	-51.9413	0.7021 ± 0.0004	rvsao-xc	Ca II H&K
SPT-CL J0205-5829	J020548.26-582848.4	31.4511	-58.4801	1.3218 ± 0.0002	rvsao-xc	Ca II H&K
SPT-CL J0205-6432	J020507.83-643226.8	31.2827	-64.5408	0.7430 ± 0.0001	rvsao-xc	Ca II H&K
SPT-CL J0233-5819	J023300.97-581937.0	38.2540	-58.3270	0.6600 ± 0.0001	rvsao-xc	Ca II H&K
SPT-CL J0234-5831	J023442.26-583124.7	38.6761	-58.5235	0.4146 ± 0.0001	rvsao-xc	[O II], Ca II H&K
SPT-CL J0240-5946	J024038.38-594548.5	40.1599	-59.7635	0.4027 ± 0.0002	rvsao-xc	Ca II H&K
SPT-CL J0245-5302	J024524.82-530145.3	41.3534	-53.0293	0.3028 ± 0.0001	rvsao-xc	Ca II H&K
SPT-CL J0254-5857	J025415.47-585710.6	43.5645	-58.9530	0.4373 ± 0.0001	rvsao-xc	Ca II H&K
SPT-CL J0257-5732	J025720.95-573254.0	44.3373	-57.5484	0.4329 ± 0.0001	rvsao-xc	Ca II H&K
SPT-CL J0317-5935	J031715.84-593529.0	49.3160	-59.5914	0.4677 ± 0.0001	rvsao-xc	Ca II H&K
SPT-CL J0433-5630	J043301.03-563109.4	68.2543	-56.5193	0.6946 ± 0.0002	rvsao-xc	Ca II H&K
SPT-CL J0438-5419	J043817.62-541920.6	69.5734	-54.3224	0.4217 ± 0.0002	rvsao-xc	Ca II H&K
SPT-CL J0449-4901	J044904.03-490139.1	72.2668	-49.0275	0.7949 ± 0.0002	rvsao-xc	Ca II H&K
SPT-CL J0509-5342	J050921.37-534212.7	77.3390	-53.7035	0.4616 ± 0.0002	template	[O II], Ca II H&K
SPT-CL J0511-5154	J051142.95-515436.6	77.9290	-51.9102	0.6488 ± 0.0002	rvsao-xc	Ca II H&K
SPT-CL J0516-5430	J051637.33-543001.5	79.1556	-54.5004	0.2970 ± 0.0002	rvsao-xc	Ca II H&K
SPT-CL J0528-5300	J052805.29-525953.1	82.0220	-52.9981	0.7670 ± 0.0002	template	Ca II H&K
SPT-CL J0534-5937	J053430.04-593653.8	83.6252	-59.6150	0.5757 ± 0.0002	rvsao-xc	Ca II H&K
SPT-CL J0551-5709	J055135.58-570828.6	87.8983	-57.1413	0.4243 ± 0.0002	rvsao-xc	Ca II H&K
SPT-CL J0559-5249	J055943.19-524926.2	89.9300	-52.8240	0.6104 ± 0.0002	template	Ca II H&K
SPT-CL J2022-6323	J202209.82-632349.3	305.5409	-63.3970	0.3736 ± 0.0001	rvsao-em	[O II]
SPT-CL J2032-5627	J203214.04-562612.4	308.0585	-56.4368	0.2844 ± 0.0002	rvsao-xc	Ca II H&K
SPT-CL J2043-5035	J204317.52-503531.2	310.8230	-50.5920	0.7225 ± 0.0005	template	Ca II H&K
SPT-CL J2056-5459	J205653.57-545909.1	314.2232	-54.9859	0.7151 ± 0.0002	rvsao-xc	Ca II H&K
SPT-CL J2058-5608	J205822.28-560847.2	314.5928	-56.1465	0.6061 ± 0.0002	rvsao-xc	[O II], Ca II H&K
SPT-CL J2100-4548	J210023.85-454834.6	315.0994	-45.8096	0.7148 ± 0.0002	template	Ca II H&K
SPT-CL J2118-5055	J211853.24-505559.5	319.7218	-50.9332	0.6253 ± 0.0002	template	Ca II H&K
SPT-CL J2124-6124	J212437.81-612427.7	321.1576	-61.4077	0.4375 ± 0.0001	rvsao-xc	Ca II H&K
SPT-CL J2130-6458	J213056.21-645840.4	322.7342	-64.9779	0.3161 ± 0.0002	rvsao-xc	Ca II H&K
SPT-CL J2135-5726	J213537.41-572630.7	323.9059	-57.4419	0.4305 ± 0.0002	rvsao-xc	Ca II H&K
SPT-CL J2136-6307	J213653.72-630651.5	324.2239	-63.1143	0.9224 ± 0.0002	rvsao-xc	Ca II H&K
SPT-CL J2138-6007	J213800.82-600753.8	324.5034	-60.1316	0.3212 ± 0.0002	rvsao-xc	Ca II H&K
SPT-CL J2145-5644	J214551.96-564453.5	326.4665	-56.7482	0.4813 ± 0.0003	rvsao-xc	Ca II H&K
SPT-CL J2146-4633	J214635.34-463301.7	326.6472	-46.5505	0.9282 ± 0.0002	rvsao-xc	Ca II H&K
SPT-CL J2146-4846	J214605.93-484653.3	326.5247	-48.7815	0.6177 ± 0.0001	rvsao-xc	Ca II H&K
SPT-CL J2148-6116	J214838.82-611555.9	327.1617	-61.2655	0.5649 ± 0.0002	rvsao-xc	Ca II H&K
SPT-CL J2155-6048	J215555.46-604902.8	328.9811	-60.8175	0.5419 ± 0.0001	rvsao-xc	Ca II H&K
SPT-CL J2248-4431	J224843.98-443150.8	342.1833	-44.5308	0.3482 ± 0.0001	rvsao-xc	Ca II H&K
SPT-CL J2300-5331	J230039.69-533111.4	345.1654	-53.5198	0.2630 ± 0.0002	rvsao-xc	Ca II H&K
SPT-CL J2325-4111	J232511.70-411213.7	351.2988	-41.2038	0.3624 ± 0.0003	rvsao-xc	Ca II H&K
SPT-CL J2331-5051	J233151.13-505154.1	352.9631	-50.8650	0.5786 ± 0.0002	rvsao-xc	Ca II H&K
SPT-CL J2332-5358	J233227.48-535828.2	353.1145	-53.9745	0.4041 ± 0.0002	rvsao-xc	Ca II H&K
SPT-CL J2337-5942	J233727.52-594204.8	354.3647	-59.7014	0.7788 ± 0.0002	template	Ca II H&K
SPT-CL J2341-5119	J234112.34-511944.9	355.3015	-51.3291	1.0050 ± 0.0005	template	Ca II H&K
SPT-CL J2342-5411	J234245.89-541106.1	355.6912	-54.1850	1.0808 ± 0.0003	template	Ca II H&K
SPT-CL J2344-4243	J234443.90-424312.1	356.1829	-42.7200	0.5981 ± 0.0008	rvsao-em	[O II]
SPT-CL J2355-5056	J235547.48-505540.5	358.9479	-50.9279	0.3184 ± 0.0002	rvsao-xc	Ca II H&K
SPT-CL J2359-5009	J235942.81-501001.7	359.9284	-50.1671	0.7709 ± 0.0003	rvsao-xc	Ca II H&K

Notes. Redshifts of individual galaxies. This is a partial listing, and the full table is available electronically. The entries listed here are the central galaxies, a subset of our observations. For each galaxy, the table lists the SPT ID of the associated cluster, a galaxy ID, right ascension and declination, the redshift z and associated uncertainty, redshift measurement method, and notable spectral features. The labels of the “ z method” column are “*rvsao-xc*” and “*rvsao-em*,” respectively, for the RVS AO cross-correlation to absorption features and fit to emission lines, and “*template*” for an in-house template-fitting method using the SDSS DR2 templates.

(This table is available in its entirety in a machine-readable form in the online journal. A portion is shown here for guidance regarding its form and content.)

measurements. These include 8 clusters that have fewer than 15 measured member redshifts,⁴⁴ as well as SPT-CL J0205-6432

with $N_{\text{members}} = 15$, for which the gapper and biweight dispersions differ by more than 1σ . Since these are not independent measurements but rather two estimates of the same quantity from the same data, we consider a 1σ discrepancy to be large and an indication that the sampling is inadequate.

⁴⁴ Once again, $N_{\text{members}} = 15$ is a somewhat arbitrary cutoff. See note at the end of Section 2.3.

Table 4
Cluster Redshifts and Velocity Dispersions

SPT ID (and Flag)	N	a ($R_{200c,SPT}$)	z	σ_{SPT} (km s^{-1})	σ_G (km s^{-1})	σ_{BI} (km s^{-1})
SPT-CL J0000-5748	26	1.0	0.7019(06)	935	598 ± 109	563 ± 104
SPT-CL J0014-4952	29	1.3	0.7520(09)	1004	812 ± 140	811 ± 141
SPT-CL J0037-5047	18	1.6	1.0262(09)	945	550 ± 121	555 ± 124
SPT-CL J0040-4407	36	0.4	0.3498(10)	1171	1275 ± 196	1277 ± 199
SPT-CL J0118-5156 \star	14	0.9	0.7050(14)	865	948 ± 239	986 ± 252
SPT-CL J0205-5829 ^a	9	1.3	1.3219(16)	1101
SPT-CL J0205-6432 \star	15	1.1	0.7436(10)	862	687 ± 167	340 ± 84
SPT-CL J0233-5819 \star	10	0.9	0.6635(14)	884	783 ± 238	800 ± 245
SPT-CL J0234-5831	22	0.3	0.4149(09)	1076	929 ± 185	926 ± 186
SPT-CL J0240-5946	25	0.4	0.4004(09)	948	999 ± 186	1014 ± 190
SPT-CL J0245-5302	30	...	0.3001(10)	...	1245 ± 210	1235 ± 211
SPT-CL J0254-5857	35	0.4	0.4371(12)	1071	1431 ± 223	1483 ± 234
SPT-CL J0257-5732	23	0.6	0.4337(12)	800	1220 ± 237	1157 ± 227
SPT-CL J0317-5935	17	0.5	0.4691(06)	832	473 ± 108	473 ± 109
SPT-CL J0433-5630	23	0.7	0.6919(15)	817	1260 ± 244	1232 ± 242
SPT-CL J0438-5419	18	0.5	0.4223(16)	1211	1428 ± 315	1422 ± 317
SPT-CL J0449-4901	20	0.6	0.7898(15)	972	1067 ± 223	1090 ± 230
SPT-CL J0509-5342	21	0.8	0.4616(07)	963	670 ± 136	678 ± 139
SPT-CL J0511-5154	15	0.9	0.6447(11)	873	778 ± 189	791 ± 194
SPT-CL J0516-5430	48	0.4	0.2940(05)	995	721 ± 96	724 ± 97
SPT-CL J0528-5300	21	1.2	0.7694(17)	857	1397 ± 284	1318 ± 271
SPT-CL J0533-5005	4	0.4	0.8813(04)	826
SPT-CL J0534-5937	3	0.4	0.5757(04)	782
SPT-CL J0546-5345 ^b	21	0.8	1.0661(18)	1080	1162 ± 236	1191 ± 245
SPT-CL J0551-5709	34	0.7	0.4243(08)	848	962 ± 152	966 ± 155
SPT-CL J0559-5249	37	0.8	0.6092(10)	1072	1135 ± 172	1146 ± 176
SPT-CL J2022-6323	37	0.4	0.3832(08)	847	1076 ± 163	1080 ± 166
SPT-CL J2032-5627	31	0.3	0.2841(06)	898	771 ± 128	777 ± 131
SPT-CL J2040-4451 ^c \star	14	1.5	1.4780(25)	989	1111 ± 280	676 ± 173
SPT-CL J2040-5725	5	0.9	0.9295(36)	890
SPT-CL J2043-5035	21	1.1	0.7234(07)	969	509 ± 104	524 ± 108
SPT-CL J2056-5459 \star	12	0.7	0.7185(12)	891	704 ± 193	642 ± 178
SPT-CL J2058-5608	9	0.9	0.6065(18)	780
SPT-CL J2100-4548	20	1.4	0.7121(11)	803	874 ± 183	854 ± 180
SPT-CL J2104-5224	23	1.5	0.7990(14)	849	1176 ± 228	1153 ± 226
SPT-CL J2106-5844 ^d	18	1.0	1.1312(21)	1287	1216 ± 268	1228 ± 274
SPT-CL J2118-5055	25	1.2	0.6249(11)	855	981 ± 182	982 ± 184
SPT-CL J2124-6124	24	0.6	0.4354(11)	916	1151 ± 218	1153 ± 221
SPT-CL J2130-6458	47	0.5	0.3164(06)	882	897 ± 120	903 ± 122
SPT-CL J2135-5726	33	0.4	0.4269(09)	976	1020 ± 164	1029 ± 167
SPT-CL J2136-4704	24	0.6	0.4247(14)	870	1461 ± 277	1461 ± 280
SPT-CL J2136-6307 \star	10	0.8	0.9258(25)	883	1244 ± 377	1269 ± 389
SPT-CL J2138-6007	34	0.3	0.3185(10)	1014	1269 ± 201	1303 ± 209
SPT-CL J2145-5644	37	0.5	0.4798(13)	1025	1634 ± 248	1638 ± 251
SPT-CL J2146-4633	18	1.0	0.9318(28)	1057	1840 ± 406	1817 ± 405
SPT-CL J2146-4846	26	0.9	0.6230(08)	872	772 ± 140	784 ± 144
SPT-CL J2148-6116	30	0.6	0.5707(09)	894	969 ± 164	966 ± 165
SPT-CL J2155-6048	25	0.9	0.5393(12)	787	1157 ± 215	1162 ± 218
SPT-CL J2248-4431	15	0.2	0.3512(15)	1417	1304 ± 317	1301 ± 320
SPT-CL J2300-5331	24	0.3	0.2623(08)	816	887 ± 168	920 ± 177
SPT-CL J2301-5546 \star	11	0.7	0.7479(22)	847	1242 ± 357	1261 ± 367
SPT-CL J2325-4111	33	0.6	0.3579(15)	1048	1926 ± 310	1921 ± 312
SPT-CL J2331-5051	78	0.9	0.5748(08)	970	1363 ± 141	1382 ± 145
SPT-CL J2332-5358	53	0.6	0.4020(08)	1016	1253 ± 158	1240 ± 158
SPT-CL J2337-5942	19	0.9	0.7764(10)	1181	700 ± 150	707 ± 153
SPT-CL J2341-5119	15	1.1	1.0025(17)	1091	1111 ± 270	959 ± 236
SPT-CL J2342-5411 \star	11	1.5	1.0746(27)	893	1278 ± 368	1268 ± 369
SPT-CL J2344-4243 ^e	32	0.7	0.5952(18)	1317	1824 ± 298	1878 ± 310
SPT-CL J2347-5158 \star	12	...	0.8693(11)	...	630 ± 173	635 ± 176
SPT-CL J2355-5056	37	0.5	0.3200(08)	856	1124 ± 170	1104 ± 169
SPT-CL J2359-5009	26	0.9	0.7747(11)	889	951 ± 173	950 ± 175

Notes. This table shows the number N ($\equiv N_{\text{members}}$) of spectroscopic members as determined by iterative 3σ clipping, the aperture radius a within which they were sampled in units of $R_{200c,SPT}$, the robust biweight average redshift z with the uncertainty in the last two digits in parentheses, the “equivalent dispersion” calculated from the SZ-based SPT mass σ_{SPT} (see Section 3.2.1), and the measured gapper scale σ_G and biweight dispersion σ_{BI} . The star flag \star in the SPT ID column indicates potentially less reliable dispersion measurements (see Section 3.2).

^a For SPT-CL J0205-5829, see also Stalder et al. (2013).

^b For SPT-CL J0546-5345, see also Brodwin et al. (2010).

^c For SPT-CL J2040-4451, see also Bayliss et al. (2013).

^d For SPT-CL J2106-5844, see also Foley et al. (2011).

^e For SPT-CL J2344-4243, see also McDonald et al. (2012).

3.2.1. The Stacked Cluster

To examine the ensemble phase-space galaxy selection, we produce a stacked cluster from our observations; this stacked cluster will also be useful for evaluating our confidence intervals via resampling (see Section 4.2). We generate it in a way that is independent of cluster membership determination. As the calculation of the velocity dispersion and membership selection are unavoidably intertwined, we use the SPT mass—the other uniform mass measurement that we have for all clusters—to normalize the velocities before stacking.

We make a stacked proper-velocity distribution independent of any measurement of the velocity dispersion by calculating the “equivalent dispersion” from the SPT mass. We convert the $M_{500c,SPT}$ to $M_{200c,SPT}$ assuming an Navarro–Frenk–White (NFW) profile and the Duffy et al. (2008) concentration, and then convert the $M_{200c,SPT}$ to a σ_{SPT} (in km s^{-1}) using the Saro et al. (2013) scaling relation. This σ_{SPT} is listed in Table 4 for reference. We also normalize the distance to the SZ center by $R_{200c,SPT}$. The resulting phase-space diagram of the normalized proper velocities v_i/σ_{SPT} versus $r_i/R_{200c,SPT}$ is shown in Figure 2. For reference, different velocity cuts are plotted. The black dashed line is a 3σ cut. The blue dotted line is a radially dependent $2.7\sigma(R)$ cut, where again the $\sigma(R)$ is from an NFW profile; this velocity cut is found to be optimal for rejecting interlopers by Mamon et al. (2010; although when considering systems without red-sequence selection). While 3σ clipping was a natural choice of membership selection algorithm (given our sometimes small sample size for individual clusters), these different cuts demonstrate that we were generally successful at selecting member galaxies. The histogram of proper velocities is shown in the right panel, together with a Gaussian of mean zero and standard deviation of one. The agreement between the distributions is difficult to quantify due to the expected presence of non-members in the histogram. We will see in Section 5 that we measure a systematic bias in normalization.

3.3. Data in the Literature: Summary and Comparison

Table 5 contains spectroscopic redshifts and velocity dispersions from the literature for clusters detected by the SPT. Notably, 14 of these clusters are from Sifón et al. (2013), which presents spectroscopic follow-up of galaxy clusters that were detected by the ACT. Because SPT and ACT are both SZ surveys based in the southern hemisphere, there is some overlap between the galaxy clusters detected with the two telescopes. We independently obtained data for five of the clusters that appear in Sifón et al. (2013), and there is some overlap between the cluster members for which we have measured redshifts. These clusters are of some interest for evaluating our follow-up strategy, because the typical number of SPT-reported member galaxies per dispersion is 25 (for $N_{\text{members}} \geq 15$), while for the overlapping Sifón et al. (2013) sample it is 55. All of the overlapping cluster redshifts and dispersions are consistent between our work and Sifón et al. (2013) at the 1σ level, except for the velocity dispersion of SPT-CL J0528-5300. Its velocity histogram shows extended structure (Figure 1). The galaxies responsible for this extended structure are kept by the membership selection algorithm in this paper, but they were either not observed or not classified as cluster members by Sifón et al. (2013). It is not possible to determine from the data in hand whether this discrepancy is statistical or systematic in origin.

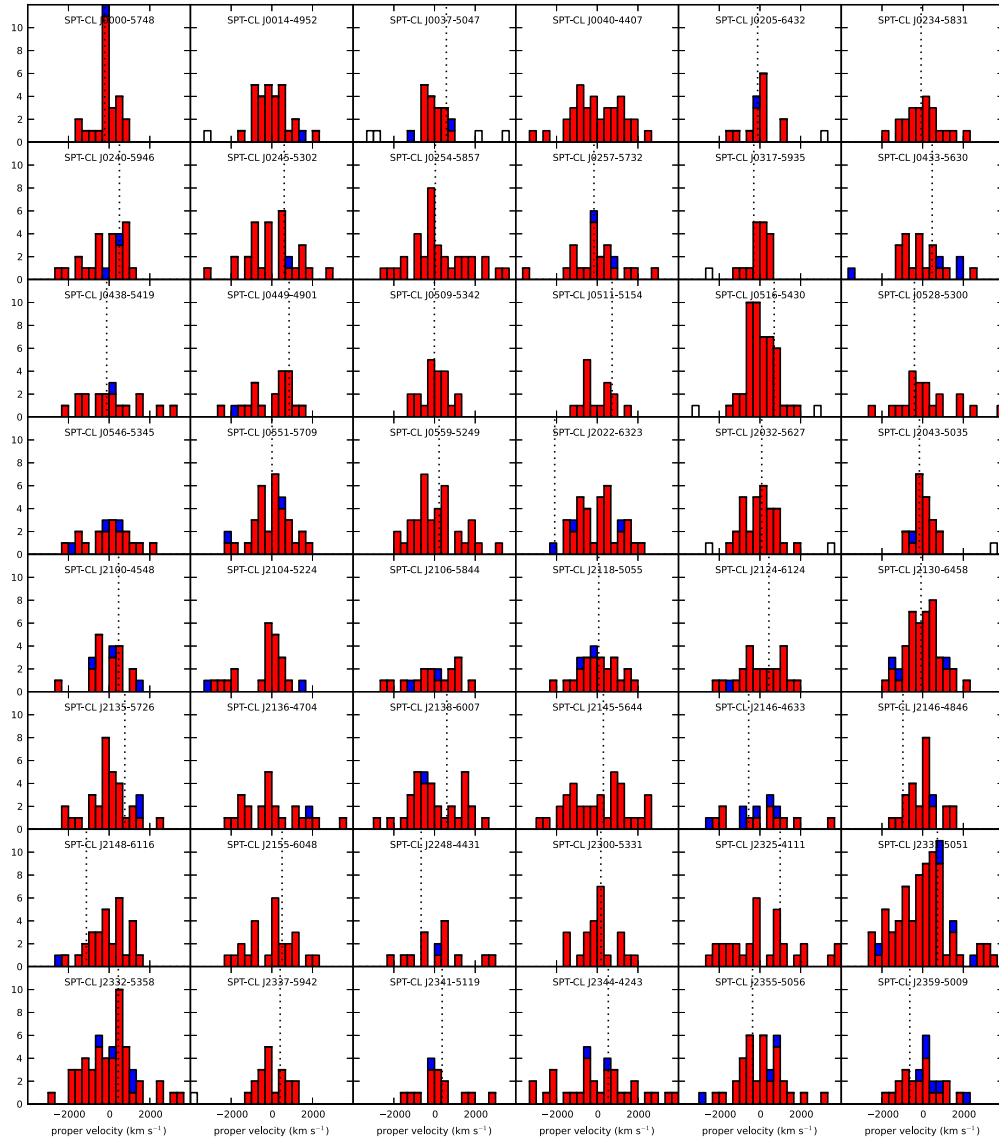


Figure 1. Histograms showing the proper velocities of galaxies selected for each cluster, where colors correspond to: (red) passive galaxies, (blue) emission-line galaxies, and (white) non-members. The central galaxy proper velocity is marked with a dotted line, though we note that this was not measured for six clusters, mostly at high redshift ($z \gtrsim 0.8$).

(A color version of this figure is available in the online journal.)

We note that ACT-CL J0616-5227, also studied in Sifón et al. (2013), is seen in SPT maps but is excluded from the survey because of its proximity to a point source.

4. STATISTICAL METHODOLOGY IN THE FEW- N_{members} REGIME

In this section, we explore the statistical issues surrounding our obtaining reliable estimates of velocity dispersions and associated confidence intervals. A key element in our approach is “resampling,” in which we extract and analyze subsets of the data, either on a cluster-by-cluster basis, or from the stacked cluster that we constructed from the entire catalog. This allows us to generate large numbers of “pseudo-observations” to address statistical questions where we have too few observations to directly answer.

4.1. Unbiased Estimators

Estimators and confidence intervals for velocity dispersions are discussed in Beers et al. (1990), which the reader is

encouraged to review. They present estimators such as the biweight, that are *resistant* and *robust*.⁴⁵ As we are exploring the properties of the few- N_{members} regime, we would also like our estimators to be *unbiased*, meaning that the mean estimate should be independent of the number of points that are sampled.

The first point that we would like to make on the subject is that the biweight dispersion (or more correctly, the associated variance) as presented in Beers et al. (1990), is biased for samples, in the same way that the population variance, $\sum_i (v_i - \bar{v})^2/n$, is biased and the sample variance, $\sum_i (v_i - \bar{v})^2/(n-1)$, is not.⁴⁶

⁴⁵ Resistance means that the estimate does not change much when a number of data points are replaced by other values; the median is a well-known example of a resistant estimator. Robustness means that the estimate does not change much when the distribution from which the data points are drawn is varied.

⁴⁶ The fact that this estimator is biased is often acknowledged by researchers who use an unbiased version of the biweight, yet cite Beers et al. (1990). Also, the implementation of the Fortran code companion to Beers et al. (1990) contains a partial correction of this bias, in a factor of $\sqrt{n/(n-1)}$ multiplying the dispersion. See rostat.f, version 1.2, 1991 February. Retrieved 2012 April from <http://www.pa.msu.edu/ftp/pub/beers/posts/rostat/rostat.f>.

Table 5
Cluster Redshifts and Velocity Dispersions from the Literature

SPT/This Work				Literature				
SPT ID	N	z	σ_{BI} (km s^{-1})	Lit. ID	N	z	σ_{BI} (km s^{-1})	Ref.
$z < 0.3$								
SPT-CL J0235-5121	ACT-CL J0235-5121	82	0.2777 ± 0.0005	1063 ± 101	1
SPT-CL J0328-5541	A3126	38	0.0844	1041	3
SPT-CL J0431-6126	A3266	132	0.0594 ± 0.0003	1182^{+100}_{-85}	2
SPT-CL J0658-5556	1E0657-56	71	0.2958 ± 0.0003	1249^{+109}_{-100}	4
SPT-CL J2012-5649	A3667	123	0.0550 ± 0.0004	1208^{+95}_{-84}	2
SPT-CL J2201-5956	A3827	22	0.0983 ± 0.0010	1103^{+252}_{-138}	5
$z \geq 0.3$								
SPT-CL J0102-4915	ACT-CL J0102-4915	89	0.8701 ± 0.0009	1321 ± 106	1
SPT-CL J0232-5257	ACT-CL J0232-5257	64	0.5559 ± 0.0007	884 ± 110	1
SPT-CL J0236-4938	ACT-CL J0237-4939	65	0.3344 ± 0.0007	1280 ± 89	1
SPT-CL J0304-4921	ACT-CL J0304-4921	71	0.3922 ± 0.0007	1109 ± 89	1
SPT-CL J0330-5228	ACT-CL J0330-5227	71	0.4417 ± 0.0008	1238 ± 98	1
SPT-CL J0346-5439	ACT-CL J0346-5438	88	0.5297 ± 0.0007	1075 ± 74	1
SPT-CL J0438-5419	18	0.4223 ± 0.0016	1422 ± 317	ACT-CL J0438-5419	65	0.4214 ± 0.0009	1324 ± 105	1
SPT-CL J0509-5342	21	0.4616 ± 0.0007	678 ± 139	ACT-CL J0509-5341	76	0.4607 ± 0.0005	846 ± 111	1
SPT-CL J0521-5104	ACT-CL J0521-5104	24	0.6755 ± 0.0016	1150 ± 163	1
SPT-CL J0528-5300	21	0.7694 ± 0.0017	1318 ± 271	ACT-CL J0528-5259	55	0.7678 ± 0.0007	928 ± 111	1
SPT-CL J0546-5345	21	1.0661 ± 0.0018	1191 ± 245	ACT-CL J0546-5345	48	1.0663 ± 0.0014	1082 ± 187	1
SPT-CL J0559-5249	37	0.6092 ± 0.0010	1146 ± 176	ACT-CL J0559-5249	31	0.6091 ± 0.0014	1219 ± 118	1
SPT-CL J2351-5452	SCSOJ235138-545253	30	0.3838 ± 0.0008	855^{+108}_{-96}	6

Notes. Number of member-galaxy redshifts N ($\equiv N_{\text{members}}$), cluster redshift, and velocity dispersion for clusters found in the literature that are also SPT detections. In the cases where we are presenting our own spectroscopic observations, some of the information from Table 4 is repeated in the left half of the present table for reference.

References. (1) Sifón et al. 2013; (2) Girardi et al. 1996; (3) Struble & Rood (1999, this paper does not contain confidence intervals); (4) Barrera et al. 2002; (5) Katgert et al. 1998; (6) Buckley-Geer et al. 2011.

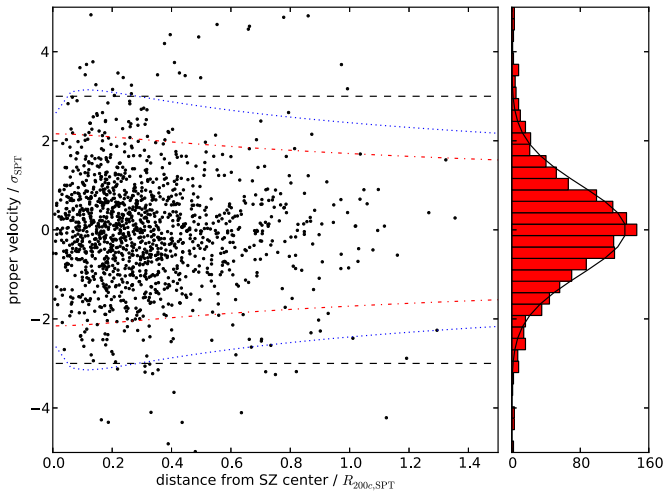


Figure 2. Stacked cluster, constructed using the dispersion equivalent to the SPT mass. Left panel: phase-space diagram of velocities. The black dashed line is a 3σ cut, and the blue dotted line is a radially dependent $2.7\sigma(R)$ cut; see the text, Section 3.2.1 for more details. These cuts would be applied iteratively in membership selection. Right panel: histogram of proper velocities, and Gaussian distribution with a mean of zero, a standard deviation of one, and an area equal to that of the histogram.

(A color version of this figure is available in the online journal.)

We use the biweight sample variance, which does not suffer from this bias (see, e.g., Mosteller & Tukey 1977):

$$\sigma_{\text{BI}}^2 = N_{\text{members}} \frac{\sum_{|u_i| < 1} (1 - u_i^2)^4 (v_i - \bar{v})^2}{D(D-1)} \quad (1)$$

where v_i are the proper velocities, \bar{v} their average,

$$D = \sum_{|u_i| < 1} (1 - u_i^2)(1 - 5u_i^2), \quad (2)$$

and u_i is the usual biweight weighting

$$u_i = \frac{v_i - \bar{v}}{9 \text{MAD}(v_i)}, \quad (3)$$

where $\text{MAD}(v_i)$ is the median absolute deviation of the velocities.

We calculate cluster redshifts using the same biweight average estimator that is presented in Beers et al. (1990). Unlike the more subtle case of the variance, the biweight average is unbiased for all N_{members} .

A second issue related to bias at few N_{members} is the possibility that the presence of velocity substructure would bias the estimation of the dispersion. We tested whether that was the case by extracting smaller pseudo-observations from the 18 individual clusters for which we obtained 30 or more member velocities. We did not use the stacked cluster here, as substructure would be lost in the averaging. For each cluster, we randomly drew 1000 pseudo-observations with $10 \leq N_{\text{members}} \leq 25$. The cluster redshift and dispersion from those smaller, random samples was computed and compared to the value that was measured with the full data set.

Figure 3 shows the results of this resampling analysis as a function of N_{members} ; the black solid line is the average relative error $\langle (\sigma_{\text{BI}} - \sigma_{\text{pseudo-obs}}) / \sigma_{\text{BI}} \rangle$ of the sample velocity dispersion of all samples across all clusters, while the colored

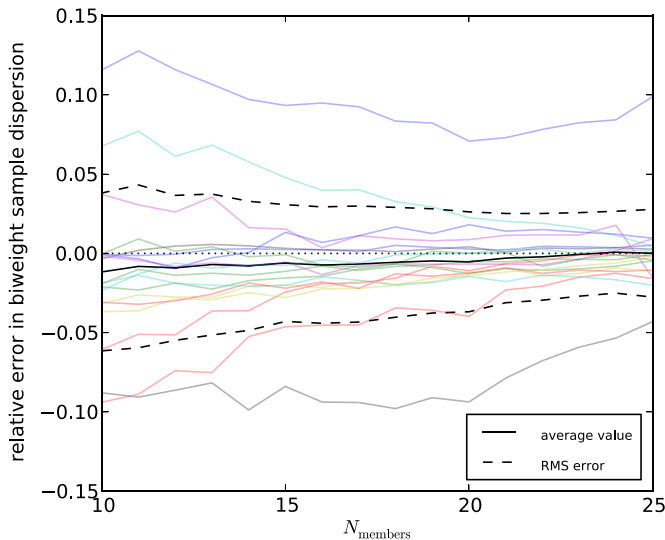


Figure 3. Average relative error $(\sigma_{\text{BI}} - \sigma_{\text{pseudo-obs}})/\sigma_{\text{BI}}$ in the measured dispersion for pseudo-observations sampled from each individual cluster with more than 30 members, as described in Section 4.1. The colored solid lines show the average across pseudo-observations for each individual cluster. The black solid line is the average across clusters, and the dashed lines show the 1σ range in the distribution of colored traces. The dotted line is identically zero. 1000 pseudo-observations were drawn with replacement at each N_{members} , and 3σ clipping membership selection was applied to each pseudo-observation before computation of the dispersion. The average relative error departs from zero at the percent level; from this we conclude that the observation of only a small number of velocities per cluster does not introduce bias in the measurement of the velocity dispersion, in an ensemble sense. However, it presents an additional source of error for individual clusters, which will increase the measurement scatter.

(A color version of this figure is available in the online journal.)

solid lines depict the average relative error for the individual clusters. The average relative error departs from zero at the percent level. From this, we conclude that the observation of only a small number of velocities per cluster does not introduce significant bias in the measurement of the velocity dispersion for an ensemble of clusters.

However, we see that for some individual clusters that have many measured galaxy velocities, the distribution of velocities is such that measuring fewer members in a pseudo-observation yields, on average, a velocity dispersion that can have several to many percent difference with the one obtained with more members. This is a way in which observing few member galaxies will increase the scatter of observed velocity dispersions at fixed mass. The size of our sample does not allow us to pursue this effect thoroughly, but Figure 3 shows that this systematic increase in the scatter is of the order of 5%, relative to dispersions computed with more than 30 members. Saro et al. (2013) isolate the scatter that is not due to statistical effects and also find that the scatter due to systematics increases at few- N_{members} and that this effect is most significant when N_{members} is less than ~ 30 .

4.2. Confidence Intervals

We now turn to the calculation of the statistical uncertainty on our measured redshifts and velocity dispersions. Beers et al. (1990) describe a number of different ways in which the confidence intervals on biweight estimators can be calculated. They conclude that the statistical jackknife and the statistical bootstrap both yield satisfactory confidence intervals. Broadly speaking, both of these methods estimate the confidence intervals by looking at the internal variability of a sample. The statistical

jackknife constructs a confidence interval for an estimate from how much it varies when data points are removed. The bootstrap generates a probability distribution function for the estimate from resampling the observed values with replacement a large number of times, often 1000 or more. The confidence intervals can then be found from the percentiles of this distribution. Many publications after Beers et al. (1990) have chosen the bootstrap; different practices seen in its use, with papers quoting asymmetric confidence intervals and others symmetric ones, have prompted us to inspect our uncertainties carefully.

The reason for using the statistical bootstrap or jackknife is the absence of an analytic expression for the distribution of the errors, given that the source distribution of velocities is unknown, as is the distribution of measured biweight dispersions. We use the stacked cluster as the best model of a cluster with our selection of potential member galaxies. As explained in Section 3.2.1, the availability of SPT masses for all clusters allows us to construct this stacked cluster independently of cluster membership determination or dispersion measurements. We draw a large number of pseudo-observations with replacement from the stacked cluster, perform member selection, and calculate the cluster’s redshift and velocity dispersion from each pseudo-observation. Thus, we generate a probability distribution function for those quantities.

We find that the distribution of the measured cluster redshift is close to a normal distribution whose standard deviation is well described by:

$$\Delta z = \frac{1}{c} \frac{\sigma_{\text{BI}}(1+z)}{\sqrt{N_{\text{members}}}}. \quad (4)$$

This is the “usual” standard error; the $1/c$ factor converts between velocity and redshift, and the $1+z$ factor is needed because σ_{BI} is defined in the rest frame. At any given N_{members} , the average bootstrap and jackknife uncertainties also reproduce this standard error.

In the case of the velocity dispersion, the bootstrap and jackknife give confidence intervals that are too narrow. Simply put, those estimators use a sample’s internal variability to infer likely properties of the population from which it was drawn. However, the variability is reduced by the membership selection, and the effect of that step is not included in the confidence interval.

The distribution of biweight sample dispersions measured in pseudo-observations after 3σ clipping membership selection is also observed to be close to a normal distribution in our resampling analysis. We set out to model the standard deviation of this distribution, which is the uncertainty that we are looking for.

If we draw observations from a normal distribution of variance σ^2 and calculate the velocity dispersion as the “usual” (non-biweight) sample standard deviation from n members, without a membership selection step, then the distribution of the measured standard deviation is related to a chi distribution with $n - 1$ degrees of freedom. Indeed, the sample standard deviation s is

$$s = \sqrt{\frac{1}{n-1} \sum_{i=1}^n (v_i - \bar{v}_i)^2}. \quad (5)$$

This implies that

$$\frac{s}{\sigma} = \sqrt{\frac{1}{n-1} \sum_{i=1}^n \frac{(v_i - \bar{v}_i)^2}{\sigma^2}} \quad (6)$$

$$\Rightarrow \sqrt{n-1} \frac{s}{\sigma} = \sqrt{\sum_{i=1}^n \frac{(v_i - \bar{v}_i)^2}{\sigma^2}} \sim \chi_{n-1} \quad (7)$$

which is the definition of a chi distribution.

The variance of the chi distribution varies very little between $k = 10$ and $k = 100$ degrees of freedom:

$$\text{Var } \chi_k = k - 2 \left(\frac{\Gamma((k+1)/2)}{\Gamma(k/2)} \right)^2 \quad (8)$$

$$= 0.49 \quad (k = 10) \quad (9)$$

$$= 0.50 \quad (k = 100). \quad (10)$$

Therefore, taking the square root on each side to find the standard deviation Δ of the dispersion estimate s:

$$\Delta \left(\sqrt{n-1} \frac{s}{\sigma} \right) = \sqrt{0.5} = 0.7 \quad (11)$$

$$\Rightarrow \Delta s = 0.7\sigma / \sqrt{n-1}. \quad (12)$$

Following the above, we model the uncertainty as

$$\Delta \sigma_{\text{BI}} = C_{\text{BI}} \sigma_{\text{BI}} / \sqrt{N_{\text{members}} - 1} \quad (13)$$

where C_{BI} is a constant. We also parameterize the uncertainty on the gapper measurement in the same way, with a constant C_{G} .

Figure 4 shows the relative error in σ_{BI} measured from the resampling analysis, as a function of N_{members} , for $10 \leq N_{\text{members}} \leq 60$. The solid black line shows the average error, and the blue dashed line is the asymmetric rms error.

We find the numerical value of C_{BI} as the mean ratio of the rms error and $1/\sqrt{N_{\text{members}} - 1}$. We find that $C_{\text{BI}} = 0.92$. The green dotted line of Figure 4 shows the uncertainty given by our model, $\pm 0.92/\sqrt{N_{\text{members}} - 1}$. Similarly for the gapper scale, we find that $C_{\text{G}} = 0.91$.

Therefore, we find that the 3σ membership selection combined with the biweight estimation of the dispersion gives an uncertainty increased by 30% compared with random sampling from a normal distribution, and also compared to the bootstrap and jackknife estimates. The larger errors are caused by non-Gaussianity in the velocity distribution and by the cluster membership selection, which can both include non-members and reject true members, generically leading to increased scatter in the measured dispersion.

We note that this effect is different than the systematic scatter shown in Figure 3, where the measured dispersion changed significantly for some individual clusters when resampling with fewer galaxy members. This latter effect likely has both physical (e.g., velocity sub-structure in the cluster) and measurement (e.g., member selection, interlopers) origins. However, both effects will be present at some level in any dispersion measurement, and the results here are important benchmarks for simulations to compare to and reproduce.

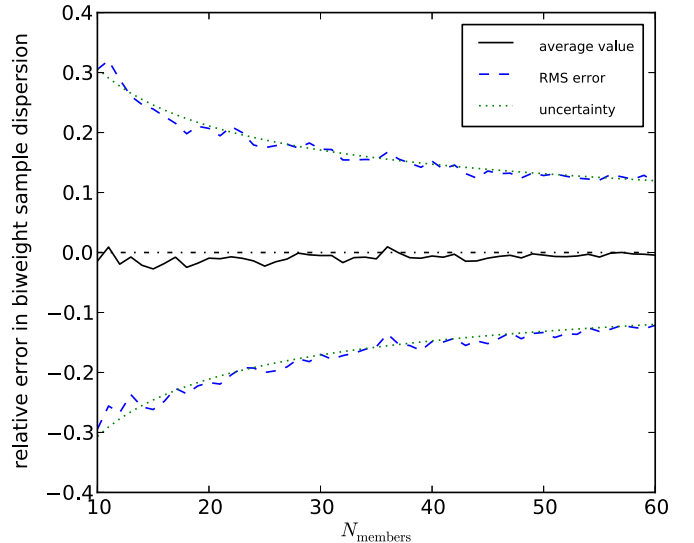


Figure 4. Statistical uncertainty and relative error in the measured dispersion for pseudo-observations sampled from the stacked cluster, as described in Section 4.2. The black solid line shows the average error, the blue dash-dotted line is the asymmetric rms error, and the green dotted line is the (relative) uncertainty, $\pm 0.92/\sqrt{N_{\text{members}} - 1}$. The parameter $C_{\text{BI}} = 0.92$ from Equation (13) was fit using this rms error, hence the agreement of the lines. The dot-dashed line is identically zero. 1000 pseudo-observations were drawn with replacement at each N_{members} , and 3σ clipping membership selection was applied to each pseudo-observation before computation of the dispersion.

(A color version of this figure is available in the online journal.)

5. COMPARISON OF VELOCITY DISPERSIONS WITH OTHER OBSERVABLES

In this section, we compare our cluster velocity dispersion measurements with gas-based observables and estimates of the cluster mass. In particular, we measure the normalization and the scatter of scaling relations between the two observables, and compare these to our expectations from simulations. We neglect effects related to the SZ cluster selection, variation of the cosmology, or potentially correlated intrinsic scatter between observables, and leave the accounting of these effects to future work. However, this comparison is still useful in understanding how our velocity dispersion mass estimates compare to those using other methods, and can also help identify systematics.

5.1. Comparison with SPT Masses

Figure 5 shows 43 cluster biweight velocity dispersions from Table 4 plotted against the masses estimated from their SPT SZ signal (combined with X-ray observations where applicable; Table 1, Section 2.1). The clusters that are included are those with $N_{\text{members}} \geq 15$ and $z \geq 0.3$, except for SPT-CL J0205-6432, which was flagged as having a potentially less reliable dispersion measurement in Section 3.2. We also plot, as a solid line, the predicted scaling between dispersion and mass from Saro et al. (2013)

$$M_{200c, \text{dyn}} = \left(\frac{\sigma_{\text{DM}}}{A \times h_{70}(z)^C} \right)^B 10^{15} M_{\odot} \quad (14)$$

where $A = 939$, $B = 2.91$, and $C = 0.33$, with negligible statistical uncertainty compared to the systematic uncertainty, whose floor is evaluated to be at 5% in dispersion (Evrard et al. 2008). σ_{DM} is the dispersion computed from dark-matter subhalos, which are identified as galaxies in simulations.

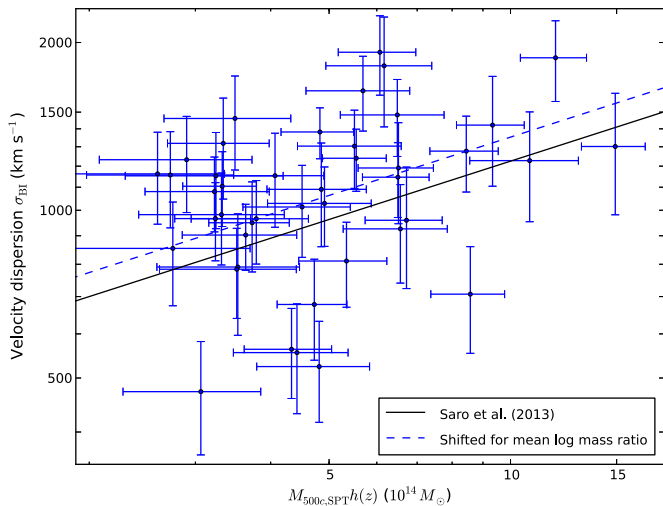


Figure 5. Cluster biweight velocity dispersions from Table 4 as a function of SZ-based SPT masses (Table 1, Section 2.1) for clusters with $N_{\text{members}} \geq 15$ and $z \geq 0.3$. The figure also shows the scaling relationship between velocity dispersion and mass expected from dark-matter simulations as a solid line (Saro et al. 2013). The dashed line is this same scaling relationship, shifted to show the average scaling relationship implied by the mean log mass ratio of the data points.

(A color version of this figure is available in the online journal.)

This has a different functional form but is consistent with the Evrard et al. (2008) scaling relation.

Our measurements appear to have a systematic offset relative to the model prediction. To quantify this offset, we compute the mean of the log mass ratio, $\ln(M_{200c, \text{dyn}}/M_{200c, \text{SPT}})$. For each cluster i , we compute this log mass ratio, and its associated uncertainty $\sigma_{\ln M_{\text{ratio},i}}$. The uncertainty in the ratio is estimated from the quadrature sum of the fractional uncertainty in the SZ and dynamical mass estimates. To the latter, we add the expected intrinsic scatter in dynamical to true mass as estimated by Saro et al. (2013):

$$\Delta_{\ln(M_{200c, \text{dyn}}/M_{200c})} = 0.3 + 0.075z. \quad (15)$$

The uncertainty on the SZ-based SPT mass already includes the effect of intrinsic scatter.

The weighted average log mass ratio is

$$\langle \ln(M_{200c, \text{dyn}}/M_{200c, \text{SPT}}) \rangle = 0.33 \pm 0.10, \quad (16)$$

where the weights for each data point are given by $1/\sigma_{\ln M_{\text{ratio},i}}^2$, and the uncertainty on the average is given by $1/\sigma^2 = \sum_i 1/\sigma_{\ln M_{\text{ratio},i}}^2$. This average log ratio means that the dynamical mass is $\exp(0.33) = 1.39$ times the SPT mass estimate.

Figure 5 shows as a dashed blue line how the N -body scaling relation is shifted if the log mass ratio is shifted by 0.33 to make the mass estimates coincide. Because the slope is $1/B = 1/2.91$, the offset in log dispersion is $(0.33 \pm 0.10)/2.91 = 0.11 \pm 0.03$. In other words, the measured velocity dispersions are on average $\exp(0.11) = 1.12$ times their expected value given the N -body simulation work and the current normalization of the SPT mass estimate. The size of this normalization offset is consistent with the expected size of systematic biases, as discussed in Section 5.3.

We quantify the level of Gaussianity in the dispersion estimates around the best-fit dispersion–mass relation by performing the Anderson–Darling test on the residuals. We find that the residuals are non-Gaussian at the 95% confidence level.

If we remove the two clusters with the lowest dispersions (SPT-CL J0317-5935 and SPT-CL J2043-5035), we find per the Anderson–Darling test that the residuals are consistent with a normal distribution. This suggests that the scatter in $\ln \sigma$ is normal—i.e., that the dispersion distribution is log-normal—with a tail toward low dispersion, as might be suspected from the distribution of data points in Figure 5.

If the statistical uncertainty on dispersion measurements of individual clusters has been correctly estimated and is much larger than any systematic uncertainty, then the fractional scatter in $\ln \sigma$ at fixed mass should roughly equal the average fractional uncertainty in the individual measurements. The mean uncertainty in log dispersion at fixed mass is 0.24, including the intrinsic scatter of the scaling relation and the uncertainty on the SPT mass. Analysis of mock observations from simulated clusters indicates that the combination of intrinsic, statistical, and systematic effects would lead to a log-normal scatter of 0.26 in dispersion at fixed mass (Saro et al. 2013). Both numbers are smaller but in general agreement with the measured scatter in $\ln \sigma$ at fixed mass, (0.31 ± 0.03) . Systematic effects can increase the scatter, as discussed in Section 5.3.

5.2. Comparison with X-Ray Observations

In this section, we compare the velocity dispersion measurements to X-ray observables and mass estimates, and contrast these results with predictions from simulations. We also compare our results to those when using a separate low-redshift sample of comparable-mass clusters with similar velocity dispersion and X-ray observables.

For the clusters in this work, we primarily use X-ray measurements from a *Chandra X-ray Visionary Project* to observe the 80 most significantly detected clusters by the SPT at $z > 0.4$ (PI: B. Benson). This cluster sample has been observed and analyzed in a uniform fashion to derive cluster mass-observables (B. A. Benson et al. 2014, in preparation) and cluster cooling properties (McDonald et al. 2013). In Table 6, we give the X-ray measured intracluster medium temperature, T_X , and the Y_X -derived cluster mass, M_{500c, Y_X} , for the 28 clusters that overlap with the sample from B. A. Benson et al. (2014, in preparation).

We also plot our results alongside velocity dispersion and X-ray measurements of comparable-mass low-redshift clusters taken from the literature. For the X-ray measurements, we use measurements of T_X and M_{500c, Y_X} from the low- z sample of Vikhlinin et al. (2009), which were produced following an analysis identical to that used in B. A. Benson et al. (2014, in preparation). The velocity dispersions for many of those galaxy clusters were calculated in a uniform way in Girardi et al. (1996). These velocity dispersion measurements were made with a different galaxy selection and more cluster members, and so will carry different systematics from our own. They nonetheless provide an interesting baseline for comparison. We will see that the scatter of those data points is smaller than that of our sample. Taking intrinsic scatter and mass uncertainties into account, the measured scatter of the literature sample at fixed mass is consistent both with our analysis from Section 4.2 and with the Girardi et al. (1996) uncertainties, and therefore is due to the lower statistical uncertainty.

Figure 6 shows the velocity dispersion versus X-ray temperature and versus M_{500c, Y_X} . The blue points are our data, and the black crosses are the data from the literature; these literature data are listed for reference in Table 6.

The left panel of Figure 6 shows dispersion versus T_X . The empirical best-fit scaling relation from Girardi et al. (1996),

Table 6
X-Ray and Velocity Dispersion Data

Cluster ID	z	N	σ_{BI} (km s $^{-1}$)	T_X (keV)	M_{500c, Y_X} ($10^{14} M_\odot$)
<i>SPT-CL</i>					
J0000-5748	0.702	26	563 \pm 104	6.75 $^{+3.09}_{-1.85}$	4.11 $^{+1.06}_{-0.80}$
J0014-4952	0.752	29	811 \pm 141	5.91 $^{+1.09}_{-0.65}$	4.97 $^{+0.54}_{-0.38}$
J0037-5047	1.026	18	555 \pm 124	2.85 $^{+1.44}_{-0.75}$	1.22 $^{+0.38}_{-0.23}$
J0040-4407	0.350	36	1277 \pm 199	5.95 $^{+1.09}_{-0.74}$	5.42 $^{+0.62}_{-0.49}$
J0234-5831	0.415	22	926 \pm 186	9.20 $^{+3.98}_{-2.52}$	6.83 $^{+1.62}_{-1.24}$
J0438-5419	0.422	18	1422 \pm 317	11.32 $^{+2.07}_{-1.76}$	10.74 $^{+1.19}_{-1.11}$
J0449-4901	0.790	20	1090 \pm 230	10.39 $^{+3.43}_{-2.53}$	6.50 $^{+1.24}_{-1.08}$
J0509-5342	0.462	21	678 \pm 139	7.28 $^{+1.30}_{-1.58}$	5.62 $^{+0.65}_{-0.72}$
J0516-5430	0.294	48	724 \pm 97	10.95 $^{+2.27}_{-1.73}$	12.25 $^{+1.52}_{-1.31}$
J0528-5300	0.769	21	1318 \pm 271	4.85 $^{+1.56}_{-0.98}$	2.68 $^{+0.50}_{-0.38}$
J0546-5345	1.066	21	1191 \pm 245	7.61 $^{+2.45}_{-1.52}$	5.22 $^{+0.98}_{-0.74}$
J0551-5709	0.424	34	966 \pm 155	3.12 $^{+0.28}_{-0.28}$	3.04 $^{+0.23}_{-0.23}$
J0559-5249	0.609	37	1146 \pm 176	6.74 $^{+0.76}_{-0.71}$	5.93 $^{+0.45}_{-0.45}$
J2043-5035	0.723	21	524 \pm 108	5.87 $^{+1.03}_{-0.63}$	4.44 $^{+0.50}_{-0.38}$
J2106-5844	1.131	18	1228 \pm 274	10.36 $^{+2.49}_{-1.79}$	8.37 $^{+1.26}_{-1.07}$
J2135-5726	0.427	33	1029 \pm 167	7.78 $^{+4.41}_{-2.10}$	5.15 $^{+1.56}_{-0.97}$
J2145-5644	0.480	37	1638 \pm 251	5.34 $^{+0.90}_{-0.74}$	5.00 $^{+0.57}_{-0.52}$
J2146-4633	0.932	18	1817 \pm 405	5.14 $^{+0.87}_{-0.82}$	3.66 $^{+0.41}_{-0.42}$
J2148-6116	0.571	30	966 \pm 165	8.24 $^{+3.14}_{-2.18}$	5.42 $^{+1.14}_{-0.93}$
J2248-4431	0.351	15	1301 \pm 320	12.37 $^{+1.01}_{-0.77}$	16.35 $^{+0.84}_{-0.70}$
J2325-4111	0.358	33	1921 \pm 312	8.84 $^{+2.16}_{-1.55}$	8.39 $^{+1.19}_{-0.98}$
J2331-5051	0.575	78	1382 \pm 145	6.38 $^{+1.84}_{-1.25}$	4.66 $^{+0.81}_{-0.66}$
J2332-5358 ^a	0.402	53	1240 \pm 158	7.40 $^{+1.20}_{-0.70}$	5.66 $^{+0.48}_{-0.48}$
J2337-5942	0.776	19	707 \pm 153	6.95 $^{+1.91}_{-1.31}$	5.76 $^{+0.92}_{-0.74}$
J2341-5119	1.002	15	959 \pm 236	9.30 $^{+2.45}_{-2.02}$	5.77 $^{+0.89}_{-0.83}$
J2344-4243	0.595	32	1878 \pm 310	11.72 $^{+2.88}_{-2.10}$	11.64 $^{+1.64}_{-1.36}$
J2355-5056	0.320	37	1104 \pm 169	4.34 $^{+1.15}_{-0.81}$	3.00 $^{+0.54}_{-0.47}$
J2359-5009	0.775	26	950 \pm 175	4.41 $^{+1.18}_{-0.65}$	2.58 $^{+0.41}_{-0.28}$
<i>Literature</i>					
A3571	0.039	70	1085 $^{+110}_{-107}$	6.81 \pm 0.10	5.90 \pm 0.06
A2199	0.030	51	860 $^{+134}_{-83}$	3.99 \pm 0.10	2.77 \pm 0.05
A496	0.033	151	750 $^{+61}_{-56}$	4.12 \pm 0.07	2.96 \pm 0.04
A3667	0.056	123	1208 $^{+95}_{-84}$	6.33 \pm 0.06	7.35 \pm 0.07
A754	0.054	83	784 $^{+90}_{-85}$	8.73 \pm 0.00	8.47 \pm 0.13
A85	0.056	131	1069 $^{+105}_{-92}$	6.45 \pm 0.10	5.98 \pm 0.07
A1795	0.062	87	887 $^{+116}_{-83}$	6.14 \pm 0.10	5.46 \pm 0.06
A3558	0.047	206	997 $^{+61}_{-51}$	4.88 \pm 0.10	4.78 \pm 0.07
A2256	0.058	47	1279 $^{+136}_{-117}$	8.37 \pm 0.24	7.84 \pm 0.15
A3266	0.060	132	1182 $^{+100}_{-85}$	8.63 \pm 0.18	9.00 \pm 0.13
A401	0.074	123	1142 $^{+80}_{-70}$	7.72 \pm 0.30	8.63 \pm 0.24
A2052	0.035	62	679 $^{+97}_{-59}$	3.03 \pm 0.07	1.84 \pm 0.03
Hydra-A	0.055	82	614 $^{+52}_{-43}$	3.64 \pm 0.06	2.83 \pm 0.03
A119	0.044	80	850 $^{+108}_{-92}$	5.72 \pm 0.00	4.50 \pm 0.03
A2063	0.034	91	664 $^{+50}_{-45}$	3.57 \pm 0.19	2.21 \pm 0.08
A1644	0.048	92	937 $^{+107}_{-77}$	4.61 \pm 0.14	4.21 \pm 0.09
A3158	0.058	35	1046 $^{+174}_{-99}$	4.67 \pm 0.07	4.13 \pm 0.05
MKW3s	0.045	30	612 $^{+69}_{-52}$	3.03 \pm 0.05	2.09 \pm 0.03
A3395	0.051	107	934 $^{+123}_{-100}$	5.10 \pm 0.17	6.74 \pm 0.18
A399	0.071	92	1195 $^{+94}_{-79}$	6.49 \pm 0.17	6.18 \pm 0.11
A576	0.040	48	1006 $^{+138}_{-91}$	3.68 \pm 0.11	2.34 \pm 0.05
A2634	0.030	69	705 $^{+97}_{-61}$	2.96 \pm 0.09	1.74 \pm 0.04
A3391	0.055	55	990 $^{+254}_{-128}$	5.39 \pm 0.19	4.06 \pm 0.10

Notes. SPT data and data from the literature used in Figure 6. For the SPT data, the redshift, number of member-galaxy redshifts ($N \equiv N_{\text{members}}$) and velocity dispersion from Table 4 are repeated for reference, and the X-ray temperature and M_{500c, Y_X} are from the same *Chandra XVP* program, except for one case that is marked. The literature clusters draw their velocity dispersion from Girardi et al. (1996) and X-ray properties from Vikhlinin et al. (2009).

^a XMM X-ray data from Andersson et al. (2011).

where $\sigma \propto T_X^{0.61}$, is plotted as a solid line; this scaling relation is consistent with the Vikhlinin et al. (2009) temperatures used here, although it was fit using X-ray temperatures from a different source, David et al. (1993). The comparison to the temperature is especially interesting in that there is, to first order, a simple correspondence between temperature and velocity dispersion. Assuming that the galaxies and gas are both in equilibrium with the potential (see, e.g., Voit 2005), then $\sigma^2 = k_B T_X / (\mu m_p)$, where m_p is the proton mass, and μ the mean molecular weight (we take $\mu = 0.58$; see Girardi et al. 1996). This energy equipartition line is plotted as a dashed line in the left panel of Figure 6. Real clusters show a deviation from this simple model, but it offers an interesting theoretical baseline, one independent of data or simulations. This relation implies that the temperature and velocity dispersion have a similar redshift evolution, which is why the quantities in this plot are uncorrected for redshift.

The X-ray Y_X observable, while not independent from T_X , is expected to be significantly less sensitive to cluster mergers than T_X , with simulations predicting Y_X to have both a lower scatter and to be a less biased mass indicator (see, e.g., Kravtsov et al. 2006; Fabjan et al. 2011). For this reason, we also plot the velocity dispersion against M_{500c, Y_X} (times a redshift-evolution factor), in the right panel of Figure 6. The dot-dashed line is the scaling relation predicted from the simulation analysis of Saro et al. (2013).

Computing the average log ratio of the dynamical and Y_X -based masses gives 0.26 ± 0.12 , corresponding to a bias of 0.09 ± 0.04 in log dispersion. This was computed, in the previous section, to be 0.33 ± 0.10 in the case of dynamical and SPT masses, corresponding to 0.11 ± 0.03 in log dispersion. The residuals of the dispersion– M_{500c, Y_X} relation have a measured scatter in dispersion of 0.31 ± 0.03 , which is the same as the measurement made using the SZ-based SPT mass. The Anderson–Darling test gives similar results to the residuals of the previous section, suggesting a normal scatter in $\ln \sigma$ with a tail toward low dispersion.

While there is very good agreement between the scaling relations comparing the dispersion to the SPT and X-ray mass estimates, we note that the results are not independent. Nine of the clusters included in this work from Reichardt et al. (2013) quoted joint SZ and X-ray mass estimates, which we have included in our sample of SPT mass estimates. In addition, the SPT significance–mass relation used in the SZ mass estimates was in part calibrated from a sub-sample of SPT clusters with X-ray mass estimates, which have effectively calibrated the SPT cluster mass normalization. Regardless, the majority of clusters in this work have SPT mass estimates derived only from the SPT SZ measurements, which have very different noise properties from the X-ray measurements, therefore the agreement in the measured scatters is not entirely trivial.

5.3. Systematics

There are two different, although related, systematics that affect the interpretation of velocity dispersion measurements: systematics that can affect the measurement of the velocity dispersion of galaxies, and a possible velocity bias between the galaxies and the underlying dark matter halo. The velocity bias cannot be empirically measured in our data. However, both effects have been quantified in recent cluster simulation studies (Saro et al. 2013; Gifford et al. 2013; Munari et al. 2013; Wu et al. 2013). In principle, the velocity bias could explain part of the offset between our measurements and the predicted relation

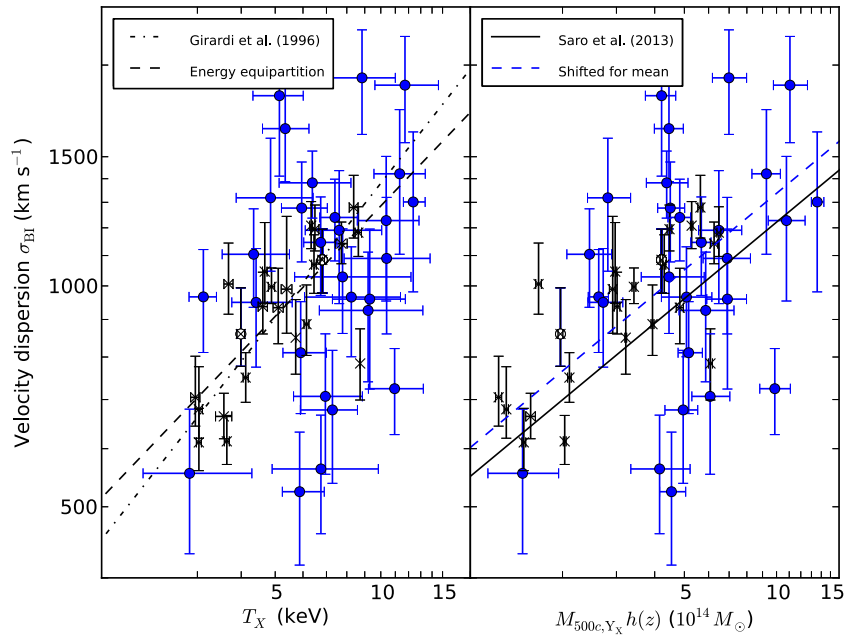


Figure 6. Velocity dispersion compared to X-ray properties. The blue points are our sample, and the black crosses are the data from the literature, with X-ray data from Vikhlinin et al. (2009) and dispersions from Girardi et al. (1996); two of them are also low-redshift SPT detections and are circled. Left panel: velocity dispersion vs. X-ray temperature. The dot-dashed line is the best-fit scaling relation from Girardi et al. (1996). The dashed line shows the scaling expected if galaxies and gas were both in equilibrium with the gravitational potential. Right panel: velocity dispersion vs. $M_{500c,YX}$. The solid line is the scaling relation from (Saro et al. 2013), and the dashed line is this same scaling relationship, shifted to show the average scaling relationship implied by the mean log mass ratio of the data points.

(A color version of this figure is available in the online journal.)

from N -body simulations, described in Sections 5.1 and 5.2. The velocity bias has been estimated to be of the order of $\sim 5\%$ by Evrard et al. (2008). More recent studies have found a spread in the velocity bias of $\sim 10\%$ when comparing different tracers and algorithms for predicting the galaxy population (Gifford et al. 2013) and comparing dark-matter with hydrodynamic simulations (Munari et al. 2013; Wu et al. 2013).

The measured velocity dispersion can be biased from the true value by the galaxy selection of the measurements, in principle being affected by systematics relating to the luminosity, color, and offset from the cluster center of the galaxies. The observations will also have some amount of imperfect membership determination, due to the presence of interlopers.

Of those effects, the luminosity of the selected galaxies has the potential to create the largest bias, according to recent simulation work showing that brighter galaxies have a smaller velocity dispersion (Saro et al. 2013; Old et al. 2013; Wu et al. 2013; Gifford et al. 2013). Observing only the 25 brightest galaxies of the halo leads to the velocity dispersion being biased low by as much as ~ 5 – 10% . These results are difficult to directly compare to our measurements, because the simulated observations use the N brightest galaxies, while real ones target a more varied population. Nonetheless, it is true that brighter galaxies are targeted in priority in our observations. As far as our data is concerned, we took the 18 clusters for which we obtained 30 or more member velocities, and compared the dispersion of the 15 brightest galaxies (among those observed spectroscopically) with our best value. The bright galaxies have a dispersion that is $(5 \pm 4)\%$ lower than the measured dispersion.

The effect of the radius at which the galaxies are sampled is discussed in Sifón et al. (2013). They conclude that there are too many uncertainties to accurately correct for a potential bias. Regardless, they estimate the systematic bias compared to sampling all the way to the virial radius by using mock

observations of a simulated cluster. They find an average correction of 0.91 to the velocity dispersions and 0.79 to the dynamical masses; in other words, the measured velocity dispersions are biased high by 10%. That a small aperture radius should bias the velocity dispersions high is in line with the results of Saro et al. (2013) and Gifford et al. (2013).

We performed a related test of the radial dependence of the dispersion using our best-sampled clusters. For the 18 clusters with 30 or more member velocities, we compared the dispersion of the half of the galaxies that are the most central with the half that are farther away from the center. There is no statistically significant difference between the most central galaxies and the most distant, their dispersions differing by $(-2 \pm 6)\%$. Our data sample cluster member galaxies out to a projected radius that is typically $\sim 0.5 \text{ Mpc } h_{70}^{-1}$, which is generally less than the virial radius. As a result, our data are not always directly comparable to the numbers quoted from the literature.

Gifford et al. (2013) also explores the effect of measuring velocity dispersion from galaxies that are a mix of red (passive) and blue (in-falling) cluster members, including blue galaxies alongside red galaxies in the spectroscopic sample, and find that including a few blue galaxies only has a small differential effect on the measured dispersion.

In addition to causing a bias in the measurement, systematics can also increase the scatter. The resampling of Section 4.1 implies that there is an increase in the scatter at few- N_{members} due to the different shapes of the velocity distribution of individual clusters. Saro et al. (2013) find that the scatter due to systematics is most significant when $N_{\text{members}} \lesssim 30$.

More feedback between statistical studies of much larger spectroscopic samples than the present one and simulation work will be needed to understand precisely how those effects affect the measured velocity dispersion. One could imagine using the color, magnitude, position, and number of the galaxies with

a spectroscopic redshift to compute a correction factor to the dispersion, or relative weights for the proper velocities, that would eliminate the systematic bias and scatter from the sources discussed above.

6. CONCLUSIONS

We have reported the first results of our systematic campaign of spectroscopic follow-up of galaxy clusters detected in the SPT-SZ survey. We have measured cluster redshifts and velocity dispersions from this data and conducted several tests to investigate the robustness of these measurements and the correlation between the velocity dispersions and other measures of cluster mass. The main findings from these tests are as follows.

1. We find our strategy of obtaining redshift and velocity dispersion estimates from a small number of galaxies per cluster (typically, $N_{\text{members}} \lesssim 30$) to be valid. By performing resampling tests that extract subsamples from a larger parent distribution, we observe no bias as a function of N_{members} in the redshift and percent-level bias in the dispersion measurements. We find, however, that the scatter is increased at few- N_{members} ; this systematic increase is due to the shapes of the velocity distribution of individual clusters (Section 4.1).
2. We fit an expression for the statistical confidence interval of the biweight dispersion after membership selection. It is given by Equation (13), and we find that $C_{\text{BI}} = 0.92$. This interval is $\sim 30\%$ larger than the intervals commonly obtained in the velocity dispersion literature by using the statistical bootstrap. The larger width is due to the membership selection step and the shape of the observed velocity distribution.
3. We compare the velocity dispersions to the SZ-based SPT mass $M_{500c,\text{SPT}}$, as well as to X-ray temperature measurements and $M_{500c,\text{X}}$. In both comparisons with a mass, the measured velocity dispersions are larger by $\sim 10\%$ on average than expected given the dispersion–mass scaling relation from dark-matter simulations and their SZ-based SPT or X-ray mass estimates. This offset is consistent with the size of several potential systematic biases in the measurement of dispersions. However, a more complete understanding of its origin should include additional measures of total mass (e.g., weak lensing), and a self-consistent analysis that includes marginalization over uncertainties in cosmology and the observable’s scaling relation with mass. We present such an analysis in Bocquet et al. (2014). The $\sim 30\%$ measured log-normal scatter in the dispersion measurements at fixed mass is slightly larger than, but generally consistent with, the expectation from simulations.

A more complete understanding of the dispersion–mass relation, which more closely coupled observationally strategies across a range of simulations, would help to reduce systematic uncertainties. Observed velocity dispersions could depend in a systematic way on the color, magnitude, and spatial selection of cluster galaxies targeted for spectroscopic measurement. Work with simulations has improved our understanding of the magnitude of systematic sources of uncertainty in velocity dispersion mass estimates, but there is has not yet been a convergence of results among different simulations. A better quantification of systematic errors will require a combination of detailed, large-volume simulations and samples of clusters with many spectroscopic members. The ultimate goal should

be a formula that maps a catalog of data—individual galaxy positions, magnitudes, colors, and recession velocities—into a cluster mass estimate that incorporates the various biases and uncertainties that result from the properties of the galaxy population that are used to estimate that cluster mass estimate. Such a formula will ultimately allow for better cosmological constraints from cluster surveys, which are currently limited by systematic uncertainties in the cluster mass calibration.

This paper includes spectroscopic data gathered with the 6.5 meter Magellan Telescopes located at Las Campanas Observatory, Chile. Time was allocated through Harvard-CfA (PIs Bayliss, Brodwin, Foley, and Stubbs) and the Chilean National TAC (PI Clocchiatti). Gemini South access was obtained through NOAO. (PI Mohr, GS-2009B-Q-16, and PI Stubbs, GS-2011A-C-3 and GS-2011B-C-6). The VLT programs were granted through DDT (PI Carlstrom, 286.A-5021) and ESO (PI Bazin, 087.A-0843, and PI Chapman, 285.A-5034 and 088.A-0902).

Optical imaging data from the Blanco 4 m at Cerro Tololo Interamerican Observatories (programs 2005B-0043, 2009B-0400, 2010A-0441, 2010B-0598) are included in this work. Additional imaging data were obtained with the 6.5 m Magellan Telescopes and the Swope telescope, which are located at the Las Campanas Observatory in Chile. This work is based in part on observations made with the *Spitzer Space Telescope* (PIDs 60099, 70053), which is operated by the Jet Propulsion Laboratory, California Institute of Technology under a contract with NASA. Support for this work was provided by NASA through an award issued by JPL/Caltech.

The South Pole Telescope program is supported by the National Science Foundation through grant ANT-0638937. Partial support is also provided by the NSF Physics Frontier Center grant PHY-0114422 to the Kavli Institute of Cosmological Physics at the University of Chicago, the Kavli Foundation, and the Gordon and Betty Moore Foundation. Galaxy cluster research at Harvard is supported by NSF grant AST-1009012. Galaxy cluster research at SAO is supported in part by NSF grants AST-1009649 and MRI-0723073. Support for X-ray analysis was provided by NASA through Chandra Award Nos. 12800071, 12800088, and 13800883 issued by the Chandra X-Ray Observatory Center, which is operated by the Smithsonian Astrophysical Observatory for and on behalf of NASA. The McGill group acknowledges funding from the National Sciences and Engineering Research Council of Canada, Canada Research Chairs program, and the Canadian Institute for Advanced Research. X-ray research at the CfA is supported through NASA Contract NAS 8-03060. The Munich group was supported by The Cluster of Excellence “Origin and Structure of the Universe,” funded by the Excellence Initiative of the Federal Government of Germany, EXC project number 153. R.J.F. is supported by a Clay Fellowship. B.A.B is supported by a KICP Fellowship, M.B. and M.M. acknowledge support from contract 2834-MIT-SAO-4018 from the Pennsylvania State University to the Massachusetts Institute of Technology. M.D. acknowledges support from an Alfred P. Sloan Research Fellowship, W.F. and C.J. acknowledge support from the Smithsonian Institution. B.S. acknowledges support from the Brinson Foundation. A.C. received support from PFB-06 CATA, Chile. This research used resources of the National Energy Research Scientific Computing Center, which is supported by the Office of Science of the U.S. Department of Energy under Contract No. DE-AC02-05CH11231.

Facilities: Blanco (MOSAIC II), Gemini-S (GMOS), Magellan:Baade (IMACS), Magellan:Clay (LDSS3), South Pole Telescope, Spitzer/IRAC, Swope, VLT:Antu (FORs2).

REFERENCES

- Allington-Smith, J., Breare, M., Ellis, R., et al. 1994, *PASP*, 106, 983
- Andersson, K., Benson, B. A., Ade, P. A. R., et al. 2011, *ApJ*, 738, 48
- Appenzeller, I., Fricke, K., Fürting, W., et al. 1998, *Msngr*, 94, 1
- Barrena, R., Biviano, A., Ramella, M., Falco, E. E., & Seitz, S. 2002, *A&A*, 386, 816
- Bayliss, M. B., et al. 2013, arXiv:1307.2903
- Beers, T. C., Flynn, K., & Gebhardt, K. 1990, *AJ*, 100, 32
- Benson, B. A., de Haan, T., Dudley, J. P., et al. 2013, *ApJ*, 763, 147
- Bocquet, S., Saro, A., Mohr, J. J., et al. 2014, *ApJ*, submitted (arXiv:1407.2942)
- Brodwin, M., Ruel, J., Ade, P. A. R., et al. 2010, *ApJ*, 721, 90
- Buckley-Geer, E. J., Lin, H., Drabek, E. R., et al. 2011, *ApJ*, 742, 48
- Danese, L., de Zotti, G., & di Tullio, G. 1980, *A&A*, 82, 322
- David, L. P., Slyz, A., Jones, C., et al. 1993, *ApJ*, 412, 479
- Desai, S., Armstrong, R., Mohr, J. J., et al. 2012, *ApJ*, 757, 83
- Dressler, A., Hare, T., Bigelow, B. C., & Osip, D. J. 2006, *Proc. SPIE*, 6269
- Duffy, A. R., Schaye, J., Kay, S. T., & Dalla Vecchia, C. 2008, *MNRAS*, 390, L64
- Evrard, A. E., Bialek, J., Busha, M., et al. 2008, *ApJ*, 672, 122
- Fabjan, D., Borgani, S., Rasia, E., et al. 2011, *MNRAS*, 416, 801
- Foley, R. J., Andersson, K., Bazin, G., et al. 2011, *ApJ*, 731, 86
- Foley, R. J., Papenkova, M. S., Swift, B. J., et al. 2003, *PASP*, 115, 1220
- Gifford, D., Miller, C., & Kern, N. 2013, *ApJ*, 773, 116
- Girardi, M., Biviano, A., Giuricin, G., Mardirossian, F., & Mezzetti, M. 1993, *ApJ*, 404, 38
- Girardi, M., Fadda, D., Giuricin, G., et al. 1996, *ApJ*, 457, 61
- Hasselfield, M., Hilton, M., Marriage, T. A., et al. 2013, *JCAP*, 7, 8
- High, F. W., Hoekstra, H., Leethochawalit, N., et al. 2012, *ApJ*, 758, 68
- High, F. W., Stalder, B., Song, J., et al. 2010, *ApJ*, 723, 1736
- Hook, I. M., Jørgensen, I., Allington-Smith, J. R., et al. 2004, *PASP*, 116, 425
- Kasun, S. F., & Evrard, A. E. 2005, *ApJ*, 629, 781
- Katgert, P., Mazure, A., den Hartog, R., et al. 1998, *A&AS*, 129, 399
- Kelson, D. D. 2003, *PASP*, 115, 688
- Komatsu, E., Smith, K. M., Dunkley, J., et al. 2011, *ApJS*, 192, 18
- Kravtsov, A. V., Vikhlinin, A., & Nagai, D. 2006, *ApJ*, 650, 128
- Kurtz, M. J., & Mink, D. J. 1998, *PASP*, 110, 934
- Mamon, G. A., Biviano, A., & Murante, G. 2010, *A&A*, 520, A30
- Marriage, T. A., Acquaviva, V., Ade, P. A. R., et al. 2011, *ApJ*, 737, 61
- McDonald, M., Bayliss, M., Benson, B. A., et al. 2012, *Natur*, 488, 349
- McDonald, M., Benson, B. A., Vikhlinin, A., et al. 2013, *ApJ*, 774, 23
- Mosteller, F., & Tukey, J. W. 1977, *Data Analysis and Regression. A Second Course in Statistics* (Reading, MA: Addison-Wesley)
- Munari, E., Biviano, A., Borgani, S., Murante, G., & Fabjan, D. 2013, *MNRAS*, 430, 2638
- Old, L., Gray, M. E., & Pearce, F. R. 2013, *MNRAS*, 434, 2606
- Planck Collaboration, et al. 2013, arXiv:1303.5089
- Planck Collaboration, et al. 2011, *A&A*, 536, A8
- Quintana, H., Carrasco, E. R., & Reisenegger, A. 2000, *AJ*, 120, 511
- Reichardt, C. L., Stalder, B., Bleem, L. E., et al. 2013, *ApJ*, 763, 127
- Saro, A., Mohr, J. J., Bazin, G., & Dolag, K. 2013, *ApJ*, 772, 47
- Sifón, C., Menanteau, F., Hasselfield, M., et al. 2013, *ApJ*, 772, 25
- Song, J., Zenteno, A., Stalder, B., et al. 2012, *ApJ*, 761, 22
- Stalder, B., Ruel, J., Šuhada, R., et al. 2013, *ApJ*, 763, 93
- Staniszewski, Z., Ade, P. A. R., Aird, K. A., et al. 2009, *ApJ*, 701, 32
- Struble, M. F., & Rood, H. J. 1999, *ApJS*, 125, 35
- Sunyaev, R. A., & Zel'dovich, Y. B. 1972, *CoASP*, 4, 173
- Vanderlinde, K., Crawford, T. M., de Haan, T., et al. 2010, *ApJ*, 722, 1180
- Vikhlinin, A., Burenin, R. A., Ebeling, H., et al. 2009, *ApJ*, 692, 1033
- Voit, G. M. 2005, *RvMP*, 77, 207
- Wade, R. A., & Horne, K. 1988, *ApJ*, 324, 411
- White, M., Cohn, J. D., & Smit, R. 2010, *MNRAS*, 408, 1818
- Williamson, R., Benson, B. A., High, F. W., et al. 2011, *ApJ*, 738, 139
- Wu, H.-Y., Hahn, O., Evrard, A. E., Wechsler, R. H., & Dolag, K. 2013, *MNRAS*, 436, 460
- Yahil, A., & Vidal, N. V. 1977, *ApJ*, 214, 347